THE CONDUCTIVE PROPAGATION OF NUCLEAR FLAMES. I.
DEGENERATE C+O AND O + Ne + Mg WHITE DWARFS[1]

F. X. TIMMES
Board of Studies in Astronomy and Astrophysics, UCO/Lick Observatory, University of California at Santa Cruz, Santa Cruz, CA 95064

AND

S. E. WOOSLEY
Board of Studies in Astronomy and Astrophysics, UCO/Lick Observatory, University of California at Santa Cruz, Santa Cruz, CA 95064; and
General Studies Group, Lawrence Livermore National Laboratory, Livermore, CA 94550

ABSTRACT

The physical properties—speed, width, and density structure—of conductive burning fronts in degenerate carbon-oxygen (C+O) and oxygen-neon-magnesium (O+Ne+Mg) compositions are determined for a grid of initial densities and compositions. Assuming a subsonic, isobaric nuclear flame, these properties are computed by four independent methods: a numerical radiation transport code which includes implicit hydrodynamics; a moving mesh diffusion code; an eigenvalue method; and a quasi-analytical, integral expression. The dependence of the physical properties of the flame on the assumed values of nuclear reaction rates, the nuclear reaction network employed, the thermal conductivity, and the choice of coordinate system are all investigated. The new results have implications for the formation of neutron stars by the accretion-induced collapse (AIC) of a white dwarf and for the production of Type Ia supernovae. The occurrence of AIC is critically dependent on the velocity of the nuclear conductive burning front and the growth rate of hydrodynamic instabilities. However, electron capture in nuclear statistical equilibrium behind the flame causes the density to increase (at constant pressure), restoring the density to its initial value some distance behind the front. There consequently exists a maximum length scale for the development of hydrodynamic instabilities. Treating the expanding area of the turbulent burning region as a fractal whose tile size is identical to the minimum unstable Rayleigh-Taylor wavelength, we find, for all reasonable values of the fractal dimension, that for initial C+O or O+Ne+Mg densities above about 9×10^9 g cm^{-3} the white dwarf should collapse to a neutron star.

Subject headings: conduction — nuclear reactions, nucleosynthesis, abundances — stars: neutron — white dwarfs

1. INTRODUCTION

Modern astronomy reveals many fascinating examples of nonlinear behavior, but few so extreme or with such far-reaching implications as the nonlinear dependence of the rate for nuclear burning upon the temperature. Ranging from the modest T^4 dependence of the pp1 hydrogen-burning cycle to silicon burning, where burning occurs at a rate roughly proportional to T^{47}, the temperature sensitivity of nuclear reaction is at the heart of many instabilities and explosive events. Such instabilities are generally of two varieties: (1) the thin-shell instability (Schwarzschild & Härm 1965), where the inability of a thin burning shell to change its radius or overlying mass significantly leads to a temperature rise at near constant pressure, and (2) nuclear runaways in degenerate matter where the pressure is also relatively insensitive to temperature.

In this first paper we restrict ourselves to the second class of astrophysical nuclear flames, in particular, those that propagate in highly degenerate matter where energy transport is dominated by electron conduction. We consider only conditions where the flame speed is very subsonic, that is, we treat deflagrations and avoid detonations. Under such circumstances the pressure has time to equilibrate across the flame, and it is appropriate to seek solutions evaluated under isobaric conditions. It turns out that this assumption results in considerable computational simplification.

As the temperature rises in such events, small initial perturbations are amplified by the exponential sensitivity of the reaction rate and energy generation to temperature. Consequently, after a brief period of time, which in the explosive cases is far shorter than the time for energy transport through the medium, the burning becomes localized with a sharp, almost discontinuous boundary between burned and unburned material. Owing to a tight coupling between energy diffusion and nuclear energy generation, this surface propagates as a wave front having many similarities to chemical combustion waves (e.g., Frank-Kamenetskii 1969; Zel'dovich et al. 1985; Kuo 1986; Ramos 1987; Williams 1988). We shall call this propagating boundary of thermonuclear activity a *nuclear flame* or simply a *flame*. In some astrophysical situations the flame is subject to instability and becomes wrinkled, the deformed geometry affecting the rate at which matter flows across the discontinuity. This instability is a subject we shall treat in § 4. Initially, however, attention is restricted to undeformed laminar flames whose properties can be calculated accurately by quasi-analytical and numerical means.

The specific astrophysical situation we have in mind is the propagation of nuclear burning in the interior of a white dwarf of nearly the Chandrasekhar mass. Interesting complications about how the initial conditions are achieved—the details of the accretion history and the brief convective stage that may precede the runaway—are ignored. We examine only the propagation of a flame that has already come to exist. As will be shown, this requires that a certain critical or "trigger" mass

---

[1] UCO/Lick Observatory Bulletin, No. 1217.

has already been given adequate energy. Our results are most applicable to the study of collapse and/or explosion in accreting dwarfs composed of mixtures of carbon, oxygen, neon, and magnesium. Later, in a second paper, we shall treat flame propagation in hydrogen and helium compositions with applicability to thin-shell helium-burning instabilities, novae, X-ray bursts, and γ-ray bursts (see also Fryxell & Woosley 1982).

A number of groups have shown that, under certain circumstances, a slowly accreting white dwarf composed either of carbon and oxygen or of neon and oxygen can collapse directly to a neutron star with little or no accompanying optical emission (Canal, Isern, & Labay 1980; Isern et al. 1983; Nomoto et al. 1979; Miyaji et al. 1980; Nomoto 1986; Canal, Isern, & Labay 1990b; Baron et al. 1987; Mayle & Wilson 1988; Woosley & Weaver 1986a; Hachisu, Eriguchi, & Nomoto 1986a, b; Nomoto & Iben 1985; Saio & Nomoto 1985; Kawai, Saio, & Nomoto 1987; Nomoto & Kondo 1991; Isern, Canal, & Labay 1991). Concurrently other groups have suggested that such collapses could give rise to brilliant γ-ray bursts visible even at cosmological distances (Paczyński 1986; Goodman 1986; Goodman, Dar, & Nussinov 1987; Paczyński 1990; Ramaty & Dar 1990 [but see Shemi & Piran 1990; Woosley & Baron 1992]) or at least to certain types of X-ray binaries (Canal et al. 1990b; van den Heuvel 1984, 1987) and the formation of millisecond pulsars (Bailyn & Grindlay 1990).

In principle, the result of accretion on a white dwarf could be either collapse to a neutron star or explosion as a supernova. The parameters determining the fate of the accreting white dwarf are its accretion rate and the speed with which the conductive deflagration propagates (Nomoto & Kondo 1991; Isern et al. 1991). White dwarfs near the Chandrasekhar mass have an adiabatic index close to 4/3, so even a small energy release can cause substantial expansion (Woosley 1990). On the other hand, if the flame speed is small enough compared with the sound speed or the central density high enough, a pressure deficit due to electron capture will induce collapse. Miyaji & Nomoto (1987) find an ignition density in a neon-oxygen white dwarf of 9.5×10^9 g cm^{-3}. Nomoto & Kondo (1991) also find an ignition density for a cold carbon-oxygen white dwarf near 10^{10} g cm^{-3}. Typical ignition densities in the hotter carbon-oxygen white dwarfs thought to make Type Ia supernovae are near 3×10^9 g cm^{-3} (Nomoto, Thielemann, & Yokoi 1984; Woosley 1990 and references therein). The radius of the unstable white dwarf is typically 1500 km, and the decision whether to collapse or explode is made during the first few hundred kilometers of propagation. Nomoto & Kondo, in particular, find that implosion will occur if the flame speed in these central regions is less than about 3% sonic, where the sound speed $c_s \approx 10^4$ km s^{-1}. Isern et al. find a higher limit, although their flame is parameterized in a different, radially dependent way. At 100 km their speed in a model that collapsed was 9% sonic. In all these calculations so far, however, the flame speed has been essentially a free parameter. It is of importance to know the correct value.

Similarly, the flame speed plays an important role in determining the properties of carbon deflagration models for Type Ia supernovae (Nomoto et al. 1984; see also Woosley & Weaver 1986b for a review). There it is important not only that the flame move fast enough to keep the star from imploding but also that a sufficient amount of burning occur in order both to give the star a high expansion velocity and to provide at least 0.5 $M_\odot$ or so of radioactive ^{56}Ni to power the light curve. Thus, at a density only several times less than con-

sidered in the case of accretion-induced collapse (AIC), one needs flame speeds that are close to sonic, i.e., about 10 times larger. The acceleration of the flame is believed to be a consequence of the Rayleigh-Taylor instability.

In this paper we compute the physical properties (speed, width, density drop, and density recovery time) of conductive burning nuclear flames by four different methods in several different compositions (variations in C, O, Ne, and Mg abundances) and for a grid of densities between 10^7 and 1.4×10^{10} g cm^{-3}. Previous studies of conductive flame speeds in degenerate dwarfs have been reported by Buchler, Colgate, & Mazurek (1979), Woosley & Weaver (1986a), Woosley (1986, 1990), and Garcia et al. (1991). The early study by Buchler et al. contains important typographical errors but is similar in approach to the dimensional analysis described in the next section (see also Landau & Lifshitz 1959). Two of our four ways of calculating the flame speed are similar to those discussed previously by Woosley, though a wider range of conditions have been examined here and two other (more accurate) techniques are explored.

In § 2 we discuss the four computational methods and the input physics used to determine the physical properties of conductive, burning nuclear flames. We present the numerical results in § 3, and in § 4 we discuss issues of flame stability and estimate an acceleration factor based upon the Rayleigh-Taylor instability. Finally, in § 4 we apply the results to the possibility of producing neutron stars via accretion-induced collapse of carbon-oxygen and neon-oxygen white dwarfs. The Appendix discusses some of the numerical issues of integrating nuclear reaction networks.

2. CALCULATION OF CONDUCTIVE FLAME PROPERTIES

2.1. Order-of-Magnitude Estimate

For a laminar front which propagates as a result of radiative diffusion or conduction, it is straightforward to obtain an order-of-magnitude estimate for the steady state width and speed of the subsonic wave front. The width of the flame, δ, can be approximated by setting the diffusion time scale,

$$\tau_{\text{diff}} \approx \frac{\delta^2}{D} \approx \frac{\delta^2}{\lambda c}, \qquad (1)$$

equal to the nuclear burning time scale,

$$\tau_{\text{burn}} \approx \frac{E}{\dot{S}}, \qquad (2)$$

where D is a characteristic thermal diffusion constant, λ is the electron mean free path, E is a characteristic energy per unit mass, and $\dot{S}$ is a typical energy generation rate. Solving for the width,

$$\delta \approx \left(\frac{\lambda c E}{\dot{S}}\right)^{1/2}, \qquad (3)$$

which immediately allows an estimate of the speed of the deflagration front (see also Landau & Lifshitz 1959):

$$v_{\text{cond}} \approx \frac{\delta}{\tau_{\text{burn}}} \approx \frac{\delta \dot{S}}{E} \approx \left(\frac{\lambda c \dot{S}}{E}\right)^{1/2}. \qquad (4)$$

If the diffusion time scale is much shorter than the nuclear burning time scale, any disturbance or preexisting waveform will diffuse away to the ambient conditions. If the converse condition is true, the disturbance will be overdriven, with both

time scales approaching equality in the steady state. Thus equality of the diffusion and nuclear burning time scale is a necessary condition for the flame to propagate in a steady state. Although based essentially on dimensional analysis, equation (4) provides very reasonable scaling relations (as compared with the more exact calculations to be described).

Applying equations (3) and (4) to the thermodynamics and compositions typical of classical novae, X-ray bursts, γ-ray bursts, and the thin-shell helium flash, Fryxell & Woosley (1982) derived estimates of the rise time for the light curve of the event. Given the relative crudeness of equations (3) and (4), these estimates are in reasonable agreement with observations. However, this calculation requires the choice of a burning temperature T_{burn}, essentially a guess, at which to evaluate the physical quantities. The nuclear energy generation rate $\dot{S}$, in particular, is sensitive to a high power of this guess. Clearly a more accurate theory of the properties of a propagating deflagration wave is desirable.

2.2. Deflagration Flame Physics

The most general line of attack in determining the physical properties of laminar, conductive nuclear flames is to solve concurrently for the hydrodynamics, nuclear kinetics, and transport properties. In one-dimensional Cartesian coordinates the Eulerian continuity equation for the composite mixture is

$$\frac{\partial \rho}{\partial t} + \frac{\partial}{\partial x}(\rho v) = 0 , \tag{5}$$

while the continuity equation for the ith isotope is

$$\rho\left(\frac{\partial Y_i}{\partial t} + v\,\frac{\partial Y_i}{\partial x}\right) + \frac{\partial}{\partial x}(\rho Y_i V_i) = \dot{R}_i . \tag{6}$$

The ith isotope has a charge of Z_i and has A_i nucleons. In equation (6) $Y_i = X_i/A_i = n_i/\rho N_A$ is the abundance variable and is subject to the condition

$$\sum_{j=1}^{N} A_j Y_j = 1 \tag{7}$$

and

$$\bar{A} = \left(\sum_{j=1}^{N} n_j A_j\right)\left(\sum_{j=1}^{N} n_j\right)^{-1} = \left(\sum_{j=1}^{N} Y_j\right)^{-1} , \tag{8}$$

which defines the mean number $\bar{A}$ of nucleons per isotope. Also in equation (6), $\dot{R}_i$ is the net reaction rate of the ith isotope for all reactions of the form $i(j, k)l$:

$$\dot{R}_i = \sum_{j,k} - Y_i Y_j \lambda_{jk}(i) + Y_l Y_k \lambda_{kj}(l) , \tag{9}$$

and V_i is the mass diffusion velocity. The λ_{jk} and λ_{kj} are the forward and reverse nuclear reaction rates, respectively. The diffusion velocities V_i are solved from the multicomponent diffusion equation which can be deduced from kinetic theory (Chapman & Cowling 1970; Burgers 1969)

$$\frac{\partial Y_i}{\partial x} = \sum_{j=1}^{N} \frac{\bar{A} Y_i Y_j}{D_{ij}}(V_j - V_i)$$
$$+ Y_i\left(\frac{A_i}{\bar{A}} - 1\right)\frac{1}{p}\frac{\partial p}{\partial x} + \frac{\rho}{p\bar{A}}\sum_{j=1}^{N} Y_i A_i Y_j A_j (f_i - f_j)$$
$$+ \sum_{j=1}^{N} \frac{\bar{A}}{\rho D_{ij}}\left(\frac{\alpha_j Y_i}{A_j} - \frac{\alpha_i Y_j}{A_i}\right)\frac{1}{T}\frac{\partial T}{\partial x} . \tag{10}$$

Equation (10) expresses the fact that diffusion processes respond to concentration, pressure, and temperature gradients and external forces such as gravity or an electric field. In equation (10), D_{ij} is the binary diffusion coefficient, α_i is the thermal diffusion coefficient, and f_i represents the external forces per unit mass. Equation (10) is linear in the diffusion velocities V_i, but only $N - 1$ of the equations are linearly independent; thus equation (10) is supplemented with the condition that there be no net mass flow relative to the center of mass:

$$\sum_{j=1}^{N} Y_j A_j V_j = 0 . \tag{11}$$

The equation of motion for the Newtonian fluid is

$$\rho\left(\frac{\partial v}{\partial t} + v\,\frac{\partial v}{\partial x}\right) = -\frac{\partial p}{\partial x} + \frac{\partial}{\partial x}\left(\frac{4}{3}\eta\,\frac{\partial v}{\partial x}\right) + \rho f , \tag{12}$$

where η is the shear viscosity. The energy equation is

$$\rho\left(\frac{\partial E}{\partial t} + v\,\frac{\partial E}{\partial x}\right) - \frac{p}{\rho}\left(\frac{\partial \rho}{\partial t} + v\,\frac{\partial \rho}{\partial x}\right)$$
$$= -\frac{\partial q}{\partial x} + \rho \dot{S} + \frac{4}{3}\eta\left(\frac{\partial v}{\partial x}\right)^2 + \rho\sum_{j=1}^{N} Y_j A_j f_j V_j . \tag{13}$$

The energy flux q in equation (13) has terms due to radiation, conduction, and diffusion:

$$q = -\sigma\,\frac{\partial T}{\partial x} + \frac{N_A \rho}{\bar{A}}\sum_{j=1}^{N} Y_j A_j B_j V_j$$
$$+ N_A kT \sum_{i,j=1}^{N}\left(\frac{Y_j \alpha_i}{A_i D_{ij}}\right)(V_i - V_j) , \tag{14}$$

where B_i is the binding energy of the ith species. The nuclear energy generation rate $\dot{S}$ in the energy equation is related to the net reaction rate $\dot{R}_i$ by

$$\dot{S} = N_A \sum_{j=1}^{N} \dot{R}_j B_j , \tag{15}$$

while σ is the conductivity due to radiation and conduction,

$$\sigma = \sigma_{rad} + \sigma_{cond} = \frac{4acT^3}{\rho}\left(\frac{1}{\kappa_{rad}} + \frac{1}{\kappa_{cond}}\right) . \tag{16}$$

Closure of the above system of equations is enforced by the equation of state $P = P(\rho, T, X)$ and $E = E(\rho, T, X)$, where X is the composition mass fraction vector.

Figures of merit for the effectiveness of mass diffusion and shear viscosity are provided by the dimensionless Lewis and Prandtl numbers. The Lewis number is defined as the ratio of energy transport to mass transport,

$$Le \equiv \frac{\sigma}{\rho C_p D} \approx \frac{10^{19}}{10^9 10^7 10^{-4}} \approx 10^7 , \tag{17}$$

while the Prandtl number is the ratio of viscous momentum transport to energy transport,

$$Pr \equiv \frac{C_p \eta}{\sigma} \approx \frac{10^7 10^7}{10^{19}} \approx 10^{-5} . \tag{18}$$

Consequently, mass diffusion and shear viscous processes are not important in determining deflagration flame properties in the interior of white dwarfs. At the surface of a white dwarf which has an accretion history, $Le \sim 100$ and diffusion and

viscous processes may be more important (Alecian & Vauclair 1983; Iben & MacDonald 1985; Woosley 1986; Iben, Fujimoto, & MacDonald 1991; Livio & Truran 1991a, b). For comparison, the molecular flames of common terrestrial chemical deflagrations have Le ~ 1 and steady state flame speeds of about 50 cm s^{-1} (Frank-Kamenetskii 1969; Ramos 1987). Here our estimate of the astrophysical diffusion coefficient was taken from Paquette et al. (1986), while the shear viscosity estimate came from Nandkumar & Pethick (1984).

To an excellent approximation, then, the ionic diffusion velocities and shear viscosity are zero. The Lewis number is then infinite, and the Prandtl number is zero. (The effects of a finite Lewis number are discussed later in this section.) With these assumptions, equations (5)–(16) simplify considerably. In a spherically symmetric, Lagrangian reference frame they reduce to those discussed and implemented in the computer code KEPLER by Weaver, Zimmerman, & Woosley (1978, hereafter WZW):

$$\frac{\partial m}{\partial r} = 4\pi r^2 \rho , \qquad (19)$$

$$\frac{dY_i}{dt} = \sum_{j,k} - Y_i Y_j \lambda_{jk}(i) + Y_l Y_k \lambda_{kj}(l) , \qquad (20)$$

$$\frac{dv}{dt} = -4\pi r^2 \frac{\partial P}{\partial m} - \frac{GM}{r^2} , \qquad (21)$$

$$\frac{dE}{dt} = -\frac{\partial L}{\partial m} - 4\pi P \frac{\partial(vr^2)}{\partial m} + \dot{S} , \qquad (22)$$

$$\dot{S} = N_A \sum_i \frac{dY_i}{dt} B_i . \qquad (23)$$

For a C+O or O+Ne+Mg composition at densities and temperatures in the vicinity of 10^{10} g cm^{-3} and 2×10^9 K, respectively, one expects from equation (3) flame widths δ on the order of 10^{-5} cm. Following Woosley (1986), spheres with mass between 10 and 100 g were constructed with very fine zoning. The spheres were initially of constant temperature and density, and the average spacing between mass zones was $\sim 10^{-6}$ cm. The outer pressure and temperature boundary conditions were then set equal to the constant internal values, simulating a small sample of an extended homogeneous region. The first 10 zones of the small sphere were then artificially incinerated, giving, as the initial condition, a temperature step function. In a time short compared with that needed for any burning to propagate, the outer boundary pressure caused the sphere to return to isobaric conditions with a small decrease in the density of the incinerated zones to compensate for the imposed temperature distribution. As energy diffused out of this region, a positive feedback loop was established between the temperature and the generation of energy by nuclear reactions. A wave began to propagate. The steady state physical properties of the isobaric, conductive flame were then determined. Solution of the microzoned hydrodynamical equations (19)–(23) is our first and most accurate method of determining a deflagration wave's characteristics (for a given nuclear reaction network). It is a method that includes any potential dynamical effects.

An additional degree of simplification can be achieved, however, without loss of accuracy, by specifying the pressure to be a constant. The assumption of an isobaric environment is physically rigorous for deflagration waves ($v_{cond}/c_s \ll 1$)

because all of the material in the vicinity of the wave front is in causal contact by sound waves. An isobaric thermodynamic condition reduces the momentum equation (21) to simply the acceleration due to gravity,

$$\frac{d^2 r}{dt^2} = -\frac{GM}{r^2} . \qquad (24)$$

The implied e-folding time for the density of the white dwarf undergoing homologous collapse (Fowler & Vogl 1964),

$$\tau_{dyn} \approx \frac{1}{(24\pi G\rho)^{1/2}} \approx \frac{446}{\rho^{1/2}} \text{ s} \approx 10^{-3} \text{ s} , \qquad (25)$$

is much greater than the diffusive time scale of equation (1), $\tau_{diff} \approx 10^{-12}$ s. Hence, gravitational effects are unimportant in determining conductive flame properties, and one may safely drop the momentum equation (21). Thus, under isobaric conditions, one need solve only the energy equation

$$\frac{dE}{dt} + P \frac{\partial(1/\rho)}{\partial t} = \frac{1}{\rho} \frac{\partial}{\partial x}\left(\sigma \frac{\partial T}{\partial x}\right) + \dot{S} , \qquad (26)$$

the continuity equation (19), and the nuclear reactions network represented by equation (20). Retention of the $P\,dV$ term turns out to be important.

The particular method used here to solve the coupled nonlinear diffusion equation (26) and the nuclear reaction equations is Newton-Raphson iteration on the Crank-Nicholson (1947) algorithm (Appendix). For this calculation we also employ a moving, adaptive mesh. That is, zones are added, deleted, and refined as the flame propagates. This strategy alleviates the need to specify a complete region for the simulation before the computation even commences and has the practical benefit of substantially saving computer time and storage. A Dirichlet boundary condition, $T = T_{cold}$, is imposed at the outer boundary, and a Neumann boundary condition, $dT/dx = 0$, representing zero heat flux, is enforced at the inner boundary. As before, a perturbing step function in temperature is taken as the initial condition, and the steady state properties of the wave are sought.

Expression (26) may also be written and solved in either cylindrical or spherical geometry. Once the flame has traveled a few times its own width, then (for the same reason that one may treat stellar atmospheres as approximately planar) we find no major differences between the steady state properties of planar, cylindrical, and spherical nuclear flames. Solution of the moving mesh diffusion equation (26) and the nuclear reaction equations is our second (and independent) method of determining the physical properties of the flame front. It is the method we shall employ to obtain most of our results.

The temporal evolution of the temperature for a typical case, obtained with the adaptive mesh diffusion code and verified with the implicit hydrodynamics code KEPLER, is given in Figure 1. While the detailed physics included in the calculation remains to be discussed, Figure 1 is representative of the numerical solutions we shall obtain. The isobaric, laminar flame is propagating to the right into a degenerate O+Ne+Mg composition which has a density of $\rho_9 = 10$. Direct sampling of the location of the front at various times shows that it is traveling in the steady state at a speed of $v_{cond} = 87.1$ km s^{-1} while maintaining a constant width $\delta = 2.28 \times 10^{-5}$ cm.
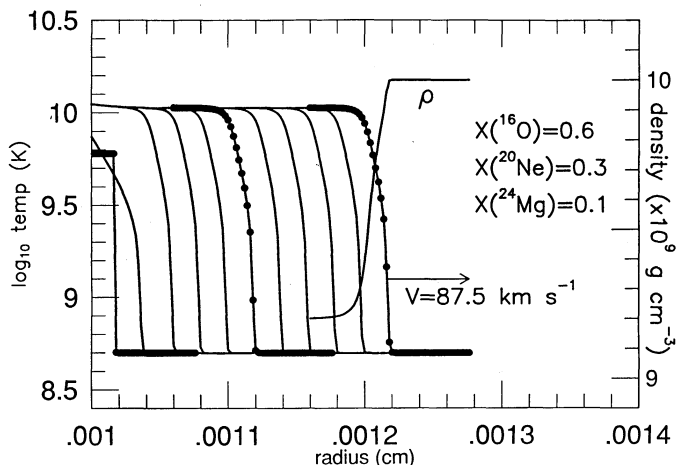
FIG. 1.—Temperature evolution of a laminar flame in degenerate O + Ne + Mg matter initially at a density of $\rho_9 = 10$. Starting from a temperature step function, a steady state wave propagates. The temperature profiles are 100 cycles apart, which is approximately equal spacing in time. The grid used in the calculation is represented by the filled circles, and the density profile corresponding to the last temperature profile calculated is shown. As expected for a subsonic deflagration wave, the density decreases behind the flame front. The entire region plotted comprises only about 10 g of material.

On the other hand, rather than seek the steady state properties of the flame by following an isobaric temporal evolution, one could assume *ab initio* the existence of a steady state wave front propagating into the cold, unburned fuel with a speed v_{cond}. The the operator replacement

$$\frac{d}{dt} \longmapsto v_{cond} \frac{d}{dx} \tag{27}$$

transforms the energy diffusion equation (26) to

$$v_{cond}\left(\frac{dE}{dx} + P\frac{d(1/\rho)}{dx}\right) = \frac{1}{\rho}\frac{d}{dx}\left(\sigma\frac{dT}{dx}\right) + \dot{S} . \tag{28}$$

The partial differential equation (26) has been transformed into the simple eigenvalue ordinary differential equation (28) having v_{cond} as its eigenvalue. There is a price to be paid for this simplification, however. With the elimination of the time derivative, hence the explicit need for specifying some initial condition, an additional boundary condition must be imposed to determine a unique solution. The choice of a Dirichlet condition $T = T_{burn}$ at the inner boundary leaves one with the undesirable situation of having to specify the final temperature T_{burn} of the material. T_{burn} is a function of the composition, the initial temperature, and the strongly nonlinear nuclear reaction rates and is therefore not a priori establishable. Once a reasonable value for T_{burn} is known, however, the solution of the eigenvalue equation (28) may be elegantly performed by using the boundary-eigenvalue techniques of Press et al. (1986). Expression (28) is our third method of determining the deflagration front properties.

Zel'dovich et al. (1985), working in the diffeomorphic arena of reactive chemical kinetics, considered the eigenvalue equation (28) in the limits of (1) a Lewis number equal to unity, (2) constant conductivity σ and specific heat at constant pressure, C_p; (3) zero $P\,dV$ work; and (4) a strict binary reaction which has an exoergic energy release that peaks very strongly at a well-defined value of the temperature, i.e., the energy gener-

ation rate $\dot{S}(T)$ goes to a delta function $\dot{S}[\delta(T - T_{burn})]$. Zel'dovich et al. were then able to derive an analytic expression for the *minimum* flame speed,

$$v_{cond} = \left[\frac{2}{\rho^2(H_{burn} - H_{cold})}\int_0^1 \frac{\sigma}{C_p}\rho\dot{S}\,dz\right]^{1/2} , \tag{29}$$

where H_{burn} and H_{cold} are the enthalpies ($H = E + P/\rho$) of the burned fuel and unburned fuel regions and z is the dimensionless enthalpy integration variable,

$$z = \frac{H - H_{cold}}{H_{burn} - H_{cold}} . \tag{30}$$

The evaluation of the nuclear energy generation rate at a single temperature, implied by the use of the delta function in assumption 4, is one reason why equation (29) is a lower bound. If the delta function approximation (assumption 4) is relaxed, Zel'dovich et al. (1985) argued that for a broad class of experimental reaction rate expressions, equation (29) remains a lower bound. The expressions for nuclear reaction rates are proportional to $\exp{(-Q/T_9^{1/3})}$ (Caughlan & Fowler 1988), which belongs to the class of expressions where equation (29) is postulated to give a lower bound.

There is another, more subtle reason why equation (29) remains a lower bound to the flame speed. Matter with a smaller $\bar{A}$ releases more energy per gram than matter with a larger $\bar{A}$ (where $\bar{A}$ is defined in eq. [8]). If assumption 1 is true, then heat and the ashes of burning the low-$\bar{A}$ matter are transported at the same rate. In the steady state, then, the energy released in the Le $\sim$ 1 flame will be less than the case where the Lewis number is very large (where fresh, low-$\bar{A}$ material is always available). The suppression of the energy generation rate in Le = 1 flames implies a smaller flame speed, by equation (4). Thus, equation (29) remains a lower bound to the flame speed even when assumption 1 is relaxed.

Failure to include $P\,dV$ terms in the energy equation artificially elevates the temperature, the corresponding nuclear energy generation rate, and, hence, by equation (4), the flame speed. The addition of $P\,dV$ work allows a zone to expand. The increased volume dilutes the thermal energy density which decreases the temperature. The energy generation rate is then suppressed, and by equation (4) the flame speed is decreased. Consequently, when assumption 3 is relaxed, the resulting flame speed is smaller than the speed given by equation (29). The detailed calculations given in § 3 show that assumption 3 yields flame speeds that are too fast by 40%. While equation (29) is not then a strict lower bound on the flame speed, it remains a useful tool.

As with the eigenvalue method, a judicious choice must be made for the burn temperature, T_{burn}, and hence the final burned enthalpy value, H_{burn}. In addition, to carry out the integration in equation (29), one must specify how the energy generation rate $\dot{S}$ varies with temperature, hence time. The approach taken by Woosley (1986) was to apply the local approximation $dT/dt = \dot{S}/C_p$, which assumes that preheating by conduction and $P\,dV$ work is unimportant within the burning region. This assumption is correct in the region where the temperature is rapidly rising (see Fig. 1) as a result of nuclear reactions, but it is incorrect either ahead of or behind this region.

It is interesting to note that in the limit that the integrand of the Zel'dovich et al. (1985) expression for the minimum flame

speed is approximately constant, the conductive speed becomes

$$v_{cond} \approx \left[\frac{\sigma \dot{S}}{\rho C_p^2 (T_{burn} - T_{cold})} \right]^{1/2} . \qquad (31)$$

Identifying the thermal diffusion coefficient D and the characteristic energy per unit mass E as

$$D \approx \frac{\sigma}{\rho C_p} \approx \lambda c , \quad E \approx C_p \Delta T \qquad (32)$$

restores equation (31) to

$$v_{cond} \approx \left(\frac{\lambda c \dot{S}}{E} \right)^{1/2} , \qquad (33)$$

which is identical to the order-of-magnitude estimate given in equation (4). The physical framework is self-consistent.

2.3. Nuclear Reaction Physics and Networks

In the first part of our study the nuclear energy generation rate $\dot{S}$ and the resulting nucleosynthesis were obtained by integrating a 19 isotope reaction network that coupled 80 nuclear reaction rates (see WZW). The tabulation of Caughlan & Fowler (1988) was employed for all critical nuclear reaction rates. With this small 19 isotope network, the results of the four methods were compared (to be discussed in the next section). To obtain an even more detailed and presumably more accurate picture of the flame's dynamics and nucleosynthesis, an arbitrary reaction network was implemented in the diffusion code. The arbitrary network is capable of extracting information from a library of about 1200 isotopes, ranging from neutrons, protons, and α-particles to ^{106}Ru. The reaction rates not prescribed by Caughlan & Fowler were taken from the reaction rate library of Woosley & Hoffman (1991).

The sensitivity of the flame's physical properties to variation in the number of isotopes in the network was investigated using five different networks: (1) a nine isotope network (Woosley 1986), (2) the 19 isotope network discussed above, (3) a 33 isotope network that removed the steady state linkages (see WZW) assumed in network 2, (4) an 83 isotope network, and (5) a 130 isotope network. The isotopes present in the five reaction networks are shown in Table 1. With the 19 and 130 isotope networks, the flame speed as a function of the assumed values of several key reaction rates was then investigated.

Nuclear reaction rate screening effects as implemented by Wallace, Woosley, & Weaver (1982) and decreases in $\dot{S}$ due to neutrino losses as given by Munakata, Koyama, & Itoh (1985) were included in the computations, although the latter were unimportant in the present context. The Appendix comments on some of the computational aspects of integrating the nuclear reaction equations as a system of ordinary differential equations and partial differential equations.

2.4. Equation of State and Transport Properties

The equation of state used in all four methods assumed Planckian photons, nonrelativistic ions, electrons having all degrees of relativity and degeneracy, and the possibility of electron pair production at elevated temperatures (see Divine 1965; Cox & Giuli 1968; Chiu 1968; Clayton 1968). In addition to these basic features, we included (1) electrostatic Coulomb corrections to the chemical potential, pressure, and internal energy in the low-temperature, high-density regime as formulated by Salpeter (1957) and (2) tables of machine precision Fermi-Dirac integrals (Cloutman 1990; Timmes 1990). For example, at $\rho = 6 \times 10^9$ ergs g^{-1}, $T = 4 \times 10^9$ K, and a mass fraction composition $X(C) = X(O) = 0.5$, a pressure $P = 5.501 \times 10^{27}$ ergs cm^{-3}, an internal energy $E = 2.492$

TABLE 1
NUCLEAR REACTION NETWORKS

ELEMENT	NET 1 ($N = 9$)		NET 2 ($N = 19$)		NET 3 ($N = 33$)		NET 4 ($N = 83$)		NET 5 ($N = 130$)	
	A_{min}	A_{max}	A_{min}	A_{max}	A_{min}	A_{max}	A_{min}	A_{max}	A_{min}	A_{max}
Neutron	1	1	1	1	1	1	1	1	1	1
H	1	1	1	1	1	3	1	3	1	3
He	4	4	3	4	3	4	3	4	3	4
C	12	12	12	12	12	12	12	12	12	14
N	...	...	...	...	14	15	14	15	13	15
O	16	16	16	16	16	16	16	18	16	19
F	...	...	...	...	...	...	19	20	18	21
Ne	20	20	20	20	20	20	19	21	19	24
Na	...	...	...	...	23	23	22	24	20	24
Mg	24	24	24	24	23	24	23	26	22	27
Al	...	...	...	...	27	27	26	28	25	29
Si	28	28	28	28	27	28	27	30	27	32
P	...	...	...	...	30	31	30	32	29	33
S	...	...	32	32	31	32	31	34	30	35
Cl	...	...	...	...	35	35	35	37	33	37
Ar	...	...	36	36	36	36	36	38	35	39
K	...	...	...	...	39	39	39	41	37	42
Ca	...	...	40	40	40	40	40	44	39	44
Sc	...	...	...	...	43	43	43	45	42	46
Ti	...	...	44	44	44	44	44	48	43	49
V	...	...	...	...	47	47	47	49	46	51
Cr	...	...	48	48	48	48	48	52	47	52
Mn	...	...	...	...	51	51	51	54	49	55
Fe	...	...	52	54	52	52	52	56	51	56
Co	...	...	...	...	55	55	55	57	53	58
Ni	56	56	56	56	56	56	56	58	54	60

$\times 10^{18}$ ergs g^{-1}, and a sound speed $c_s = 1.099 \times 10^9$ cm s^{-1} result.

In the usual situation, the temperature, density, and composition are given, and one computes the resulting pressure and internal energy. Given the pressure instead of the density, the density is obtained by iteration. Obtaining the density solution can be a significant portion of the computational cost in cases where the number of isotopes being evolved is relatively small.

With mass diffusion, shear viscosity, and gravity being unimportant to deflagration flames, the thermal conductivity becomes the most important transport property to be modeled. The average velocity of the electrons in the plasma is much greater than that of the ions, so the electrons are responsible for heat conduction. At densities appropriate to low-mass stellar remnants, the plasma is a very collisional system, that is, the collision time between particles is very short. Hence the ions and electrons have the same temperature. There is no need for considering a two-temperature plasma. The Coulomb field of the ions, whether the ions are in the liquid or the solid state, is strong enough to scatter the electrons. Degeneracy reduces the number of unoccupied electron states, which implies that the mean free path of the electrons increases. Both phenomena, then, namely, relativity (which increases the speed of the electrons) and degeneracy, increase the thermal conductivity ($\alpha \propto \lambda \bar{v}$).

Many studies have been done on the thermal conductivity of degenerate and relativistic plasmas (Lee 1950; Hubbard 1966; Hubbard & Lampe 1969; Canuto 1970; Flowers & Itoh 1976; Yakovlev & Urpin 1980; Urpin & Yakovlev 1980; Itoh et al. 1983; Nandkumar & Pethick 1984; Yakovlev 1987). Yakovlev & Urpin (1980, hereafter YU) wrote the thermal conductivity of a Fermi gas as

$$\sigma = \frac{\pi^2 k^2 T n_e}{3 m_* v} , \qquad (34)$$

where m_* is the effective electron mass,

$$m_* = \frac{p_F}{v_F}$$
$$= \left[m_e^2 + \left(\frac{p_F}{c} \right)^2 \right]^{1/2}$$
$$\simeq m_e \left[1 + \frac{\hbar^2}{m_e^2 c^2} (3\pi^2 n_e)^{2/3} \right]^{1/2}$$
$$= m_e (1 + x^2)^{1/2} ; \qquad (35)$$

n_e is the electron number density; and v is the collision frequency. The dominant source of the thermal conductivity in the interior of white dwarfs and on the surfaces of neutron stars is the inelastic scattering of electrons by ions (also known as Mott scattering). YU wrote the ion-electron collision frequency in the form

$$v_{ei} = \frac{4 e^4 m_e \bar{Z} \Lambda_{ei}}{3 \pi \hbar^3} (1 + x^2)^{1/2} , \qquad (36)$$

where Λ_{ei} is the Coulomb integral and numerically is of order unity. YU derived an analytic formula for the Coulomb integral,

$$\Lambda_{ei} = \ln \left[\left(\frac{2}{3} \pi \bar{Z} \right)^{1/3} \left(1.5 + \frac{3}{\Gamma} \right)^{1/2} - \frac{x^2}{2(1 + x^2)} \right], \qquad (37)$$

where Γ is the standard dimensionless plasma coupling parameter.

Subsequent work by Itoh et al. (1983), Nandkumar & Pethick (1984), and Yakovlev (1987) differs only in physics of the Coulomb integral. Itoh et al. and Nandkumar & Pethick included one-loop corrections to the static longitudinal dielectric function. Yakovlev (1987) considered the first term in an expansion away from the Born approximation. The 20% differences between the calculations of the various groups represents the theoretical uncertainty. In this paper we adopt the parameterized fit of Itoh et al. for the Coulomb integral.

In the low-$\bar{Z}$ ($\bar{Z} \lesssim 15$) environment of the C+O and O+Ne+Mg white dwarf, electron-electron scattering is not negligible (YU) and serves to decrease the total thermal conductivity. The electron-electron collision frequency derived by YU is

$$v_{ee} = 0.511 T^2 \frac{x^{3/2}}{(1 + x)^{5/4}} J(y) , \qquad (38)$$

where

$$y = \frac{3^{1/2} T_{pe}}{T} \qquad (39)$$

and

$$T_{pe} = \frac{\hbar \omega_{pe}}{k} = \frac{\hbar e}{k} \left[\frac{4 \pi n_e}{m_e (1 + x^2)} \right]^{1/2} . \qquad (40)$$

The function $J(y)$ takes into account the degeneracy and relativistic effects and is expressed in YU as a double integral. YU obtained analytic forms for $J(y)$ in the asymptotic limits $y \ll 1$ and $y \gg 1$ (the latter in terms of a Riemann zeta function). We found it preferable to evaluate the double integral numerically and fit a cubic spline to the results (Timmes 1992).

The thermal conductivity in the solid phase due to electron-phonon scattering has been calculated by Flowers & Itoh (1976), YU, and Raikh & Yakovlev (1982), and near the melting point by Itoh et al. (1983). Considerable disagreement (factors ~ 3) still exist between the various calculations. For convenience the analytical expression of YU, valid in the regime where the temperature is much greater than the crystals' Debye temperature,

$$\sigma_{ep} = \frac{(3\pi)^{1/3} \pi^2 \hbar^3 k}{6 m_e e^2 u_{-2}} n_e^{4/3} (1 + 0.5 x^2)^{-1} \qquad (41)$$

is adopted. The factor u_{-2} is related to the mean square thermal displacement of the ions, and the value $u_{-2} = 13$ (Pollock & Hansen 1973) is also assumed. The total electron conductivity is then calculated as

$$\frac{1}{\sigma_{\text{cond}}} = \frac{1}{\sigma_{ei}} + \frac{1}{\sigma_{ee}} + \frac{1}{\sigma_{ep}} . \qquad (42)$$

The photon opacity is composed of two additive pieces, the Compton opacity and the free-free (inverse bremsstrahlung) opacity. Compton opacities have been calculated by Sampson (1959) for Boltzmann electrons, by Chin (1965) for fermionic electrons, and by Buchler & Yueh (1976) without the assumptions made by Chin. In our work the approximation formula given in WZW, which includes a Compton cutoff for frequencies less than the plasma frequency, is adopted. The results of Buchler & Yueh are valid in the partially degenerate regime $\rho_6 \lesssim 1$. At greater densities the ability of photons to transport

energy becomes rapidly overshadowed by the electron thermal conductivity and plasma-neutrino losses when the electron degeneracy builds up. The errors incurred by extrapolating Buchler & Yueh results to the thermodynamic conditions present in the white dwarf are presumably inconsequential.

Recently Itoh, Kojo, & Nakagawa (1990) have calculated frequency-dependent Gaunt factors in the temperature and density domain of interest. When these Gaunt factors are used along with a Kramers opacity (Clayton 1968, eq. [3-170]), we estimate that the free-free opacity is the largest contributor to the photon opacity in the interiors of $C+O$ and $O+Ne+Mg$ white dwarfs. This ensures that the primary mode of energy transport is by electrons. For example, at $\rho = 6 \times 10^9$ ergs g^{-1}, $T = 4 \times 10^9$ K, and a mass fraction composition $X(C) = X(O) = 0.5$, the radiative opacity is $\kappa_{rad} = 5.616 \times 10^{-2}$ cm^2 g^{-1}, while the conductive opacity is $\kappa_{cond} = 1.587 \times 10^{-4}$ cm^2 g^{-1}. The deflagration wave's speed, width, and other properties are controlled by the thermal conductivity of the relativistic, degenerate electrons.

3. RESULTS OF THE FLAME PROPAGATION CALCULATIONS

3.1. Comparison of the Methods

The conductive flame speeds were computed over a grid of initial densities (i.e., the density in the unburned region) for both a $C+O$ and an $O+Ne+Mg$ composition by each of our four methods. The results are given in Table 2. The difference between the speeds as computed by the microzoned hydrodynamic method (col. [3]) and the energy diffusion method (col. [4]) is less than 2% in all cases. It should be stressed that these two methods of computing the conductive flame properties are independent and "fundamental" in that only the correctness of the input physics is assumed.

If one makes the adroit choice of a burn temperature (honed by experience and hindsight) $T_{9,burn} = 4.3$ for the $C+O$ composition and $T_{9,burn} = 5.3$ for the $O+Ne+Mg$ composition (independent of density), then the eigenvalue method (col. [4]) differs from the microzoned hydrocode or diffusion methods by less than 5%. However, the radius of convergence about this particular choice of burn temperature is small. For example, the choice $T_{9,burn} = 4.8$ gives speeds that differ from

the hydrocode method by about 50%, while for $T_{9,burn} = 5.3$ the eigenvalue method does not converge. While the following line of attack was not pursued, it might be noted that a popular strategy used in the study of reactive chemical flows (Ramos 1987) is to solve the time-dependent equations for a few time steps to move the final burn temperature into its radius of convergence and then apply the eigenvalue method. Thus, while not as physically fundamental as the two previous methods, the eigenvalue method is capable of computing reasonable properties of the burning deflagration front.

The entries for the minimum speed (col. [5]) were obtained using the approximations discussed in § 2, with the integrations carried out until the nuclear energy generation became negative due to photodisintegration of the heavy nuclei. The computed lower bound of the conductive speed appears to give reasonable results, in that the actual flame speed is in fact always greater than the lower bound. It is interesting that, as the density decreases, the flame speed appears to converge toward the lower bound.

In what follows, all of the quantitative results presented in the ensuing discussion will be based on both diffusion and hydrodynamical methods. Unless otherwise stated, the same results were obtained independently using both methods.

The conductive flame speed as a function of density for three different $C+O$ compositions are shown in Figure 2a. In Figure 2b the speeds are shown for three different $O+Ne+Mg$ compositions. Using a standard Levenberg-Marquardt minimization routine, the formula

$$v_{cond} = 92.0 \left(\frac{\rho}{2 \times 10^9} \right)^{0.805} \left[\frac{X(^{12}C)}{0.5} \right]^{0.889} \text{km s}^{-1} \quad (43)$$

fits the computed $C+O$ flame speeds to about 10% in the density range $0.01 \le \rho_9 \le 10$ and is consistent with the results of Woosley (1986), while the formula

$$v_{cond} = 51.8 \left(\frac{\rho}{6 \times 10^9} \right)^{1.06} \left[\frac{X(^{16}O)}{0.6} \right]^{0.688} \text{km s}^{-1} \quad (44)$$

fits the $O+Ne+Mg$ compositions to within about 12% in the density range $1 \le \rho_9 \le 14$. A more accurate fit could be

TABLE 2

COMPARISON OF METHODS USED TO CALCULATE CONDUCTIVE NUCLEAR FLAME SPEEDS[a]

Composition (1)	ρ_9 (2)	Microzone Hydrocode (3)	Diffusion Equation (4)	Eigenvalue Equation (5)	Minimum Integral (6)
$X(^{12}C) = 0.5, X(^{16}O) = 0.5$	10.0	259	259	236	98.0
	8.0	210	206	201	84.9
	6.0	172	170	165	70.2
	4.0	115	112	107	52.8
	2.0	59.6	60.3	54.9	31.1
	1.0	31.5	32.6	28.7	18.2
	0.5	16.2	16.5	12.7	11.6
	0.2	6.09	6.28	5.19	3.17
$X(^{16}O) = 0.6, X(^{20}Ne) = 0.3$	14.0	102	109	110	63.7
	12.0	101.7	98.3	96.9	57.5
	10.0	71.9	83.4	87.7	50.4
	8.0	61.0	60.2	67.5	21.2
	6.0	48.3	49.6	54.4	35.0
	4.0	27.4	28.2	36.3	25.8
	2.0	12.2	11.5	18.2	10.7
	1.0	4.91	5.06	7.88	4.62

[a] The entries were computed with the 19 isotope network listed in Table 1. All the flame speeds are in km s^{-1}.
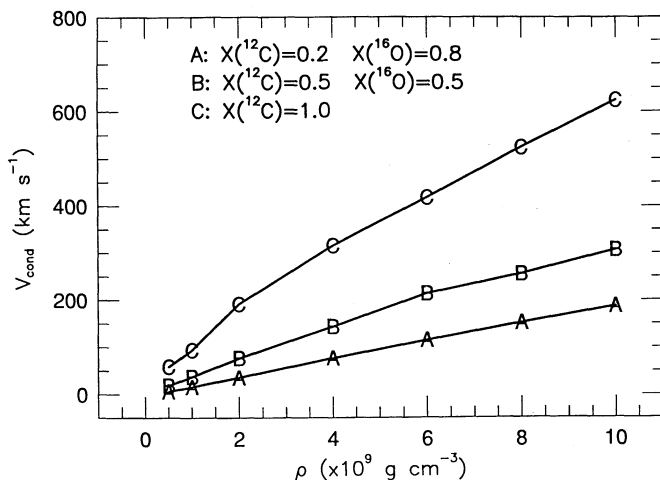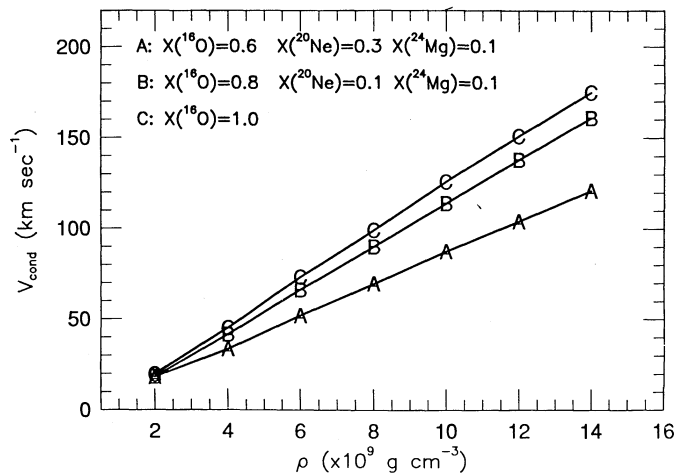
FIG. 2a

FIG. 2b

FIG. 2.—Conductive flame speed as a function of density for (a) three different C + O mixtures and (b) three different O + Ne + Mg mixtures. Letters indicate the points generated by the reactive diffusion and hydrodynamical code KEPLER. Fits to the curves are given in eqs. (43) and (44), while the exact values are presented in Tables 3 and 4.

achieved by spline-fitting the entries in Tables 3 and 4. Taken together, Figures 2a and 2b indicate that greater conductive flame speeds are achieved with material that has a higher density and a lower mean number of nucleons $\bar{A}$ (or a lower mean charge $\bar{Z}$). Expressions (22) and (23) are quite useful for determining the conductive flame speed in applications where resolving the flame front would be impractical computationally (essentially all numerical calculations of astrophysical interest).

Tables 3 and 4 provide a summary of the physical properties of the conductive burning fronts for the C + O and O + Ne + Mg compositions investigated.

TABLE 3
CARBON-OXYGEN CONDUCTIVE WAVE PROPERTIES[a]

Composition	ρ_9	v_{cond}	Width	$\Delta\rho/\rho$	t_{recov}	λ_{max}	λ_{min}
$X(^{12}C) = 0.2, X(^{16}O) = 8.0$	10.0	187	1.27 (−5)	0.085	6.78 (−2)	12.7	18.5
	8.0	152	1.65 (−5)	0.090	1.26 (−1)	19.2	14.4
	6.0	115	2.50 (−5)	0.098	2.94 (−1)	33.8	10.1
	4.0	76.3	4.96 (−5)	0.111	1.14 (+0)	87.0	5.92
	2.0	35.3	1.85 (−4)	0.139	1.47 (+1)	519	2.01
	1.0	15.1	7.28 (−4)	0.205	5.78 (+2)	8.73 (+3)	0.500
	0.5	5.46	2.79 (−3)	0.222	1.75 (+3)	9.56 (+3)	0.121
	0.2	1.09	2.03 (−2)	0.398	8.99 (+3)	9.80 (+3)	8.96 (−3)
	0.1	0.415	8.11 (−1)	0.415	...	...	1.87 (−3)
	0.05	0.113	2.31	0.483	...	...	2.38 (−4)
	0.01	9.82 (−3)	8.68	0.503	...	...	8.62 (−6)
$X(^{12}C) = 0.5, X(^{16}O) = 0.5$	10.0	307	1.06 (−5)	0.094	7.61 (−2)	23.3	45.0
	8.0	256	1.36 (−5)	0.100	1.42 (−1)	36.4	36.7
	6.0	214	1.82 (−5)	0.104	3.32 (−1)	71.1	33.0
	4.0	143	3.20 (−5)	0.122	1.28 (+0)	183	18.9
	2.0	75.8	9.35 (−5)	0.152	1.68 (+1)	1.27 (+3)	8.48
	1.0	36.4	2.89 (−4)	0.192	5.78 (+2)	2.10 (+4)	3.10
	0.5	18.1	9.46 (−4)	0.242	1.85 (+3)	3.35 (+4)	1.22
	0.2	6.15	1.08 (−2)	0.418	8.42 (+3)	5.18 (+4)	0.203
	0.1	2.33	2.75 (−2)	0.426	...	...	5.73 (−2)
	0.05	0.599	5.19 (−1)	0.486	...	...	6.64 (−3)
	0.01	4.73 (−2)	4.22	0.504	...	...	1.99 (−4)
$X(^{12}C) = 1.0, X(^{16}O) = 0.0$	10.0	624	5.57 (−6)	0.103	8.51 (−2)	53.1	170
	8.0	525	7.08 (−6)	0.107	1.60 (−1)	84.0	145
	6.0	418	8.58 (−6)	0.114	3.98 (−1)	166	114
	4.0	315	1.44 (−5)	0.132	1.45 (+0)	457	84.2
	2.0	191	3.74 (−5)	0.170	1.92 (+1)	3.67 (+3)	48.5
	1.0	93.0	1.16 (−4)	0.212	5.79 (+2)	5.39 (+4)	18.4
	0.5	58.1	3.78 (−4)	0.264	1.80 (+3)	1.05 (+5)	11.5
	0.2	15.7	1.36 (−3)	0.342	8.11 (+3)	1.27 (+5)	1.62
	0.1	6.34	4.94 (−3)	0.388	...	...	0.624
	0.05	2.42	8.62 (−3)	0.407	...	...	0.129

[a] The entries were computed with the 130 isotope network listed in Table 1 and the moving mesh diffusion code; ρ_9 is in units of 10^9 g cm^{-3}, V_{cond} in km s^{-1}, width in cm, t_{recov} in s, λ_{max} in km, and λ_{min} in (100 km)$^{-1}$. Numbers in parentheses are powers of 10.

TABLE 4

OXYGEN-NEON-MAGNESIUM CONDUCTIVE WAVE PROPERTIES[a]

Composition	ρ_9	V_{cond}	Width	$\Delta\rho/\rho$	t_{recov}	λ_{max}	λ_{min}
$X(^{16}O) = 0.6, X(^{20}Ne) = 0.3$	14.0	121	1.39 (−5)	6.69 (−2)	2.29 (−2)	2.77	7.03
	12.0	104	1.78 (−5)	7.05 (−2)	3.42 (−2)	3.56	5.75
	10.0	87.5	2.27 (−5)	7.41 (−2)	5.95 (−2)	5.21	4.64
	8.0	69.6	3.35 (−5)	7.95 (−2)	1.06 (−1)	7.38	3.42
	6.0	51.9	5.01 (−5)	8.62 (−2)	2.49 (−1)	12.9	2.44
	4.0	33.6	1.18 (−4)	0.100	9.81 (−1)	32.9	1.27
	2.0	18.2	4.31 (−4)	0.127	1.25 (+1)	227	0.588
	1.0	6.36	1.50 (−3)	0.157	6.94 (+2)	4410	0.116
$X(^{16}O) = 0.8, X(^{20}Ne) = 0.1$	14.0	161	1.12 (−5)	6.83 (−2)	2.32 (−2)	3.73	12.2
	12.0	138	1.35 (−5)	7.12 (−2)	3.50 (−2)	4.83	10.0
	10.0	114	1.74 (−5)	7.50 (−2)	5.81 (−2)	6.62	7.78
	8.0	90.2	2.66 (−5)	8.07 (−2)	1.08 (−1)	9.74	5.66
	6.0	66.2	3.93 (−5)	8.77 (−2)	2.54 (−1)	16.8	3.75
	4.0	41.7	9.80 (−5)	0.101	9.67 (−1)	40.3	1.93
	2.0	18.3	4.06 (−4)	0.128	1.27 (+1)	232	0.588
	1.0	7.12	1.40 (−3)	0.160	3.85 (+2)	2740	0.143
$X(^{16}O) = 1.0, X(^{20}Ne) = 0.0$	14.0	175	1.02 (−5)	7.24 (−2)	2.47 (−2)	4.32	13.6
	12.0	151	1.22 (−5)	7.54 (−2)	3.70 (−2)	5.59	11.3
	10.0	126	1.58 (−5)	7.92 (−2)	6.12 (−2)	7.71	9.02
	8.0	99.3	2.38 (−5)	8.49 (−2)	1.14 (−1)	11.3	6.53
	6.0	73.2	3.60 (−5)	9.20 (−2)	2.67 (−1)	20.2	4.36
	4.0	45.3	9.19 (−5)	0.106	1.03 (+0)	46.6	2.18
	2.0	19.7	3.41 (−4)	0.133	1.33 (+1)	262	0.658
	1.0	8.22	1.27 (−3)	0.165	5.31 (+2)	436	0.184

[a] The entries were computed with the 130 isotope network listed in Table 1 and the moving mesh diffusion code; ρ_9 is in units of 10^9 g cm^{-3}, V_{cond} in km s^{-1}, width in cm, t_{recov} in s, λ_{max} in km, and λ_{min} in (100 km)$^{-1}$.

3.2. The Critical Temperature and Flame Sensitivities

In steady state, the left-hand side of equation (26) is zero. The temperature where the energy generation rate $\dot{S}$ is equal to the energy conduction term

$$\frac{\partial}{\partial x}\left(\sigma\frac{\partial T}{\partial x}\right) = \rho\dot{S} \qquad (45)$$

is an important diagnostic point, called the critical temperature, T_{crit}. Any nuclear flame that is to propagate in the steady state must at least be capable of achieving the critical temperature. The nuclear energy generation rate and the energy conduction term are plotted as a function of distance for a C+O mixture in Figure 3a, and in Figure 3b for an O+Ne+Mg mixture. The spike in the energy conduction curves arises from preheating as the very sharp temperature gradient in the wave moves into the cold material. Also shown in Figures 3a and 3b is the temperature profile as a function of distance. The critical temperature T_{crit} is about 5×10^9 at this density for the C+O mixture and about 7×10^9 for the O+Ne+Mg composition.
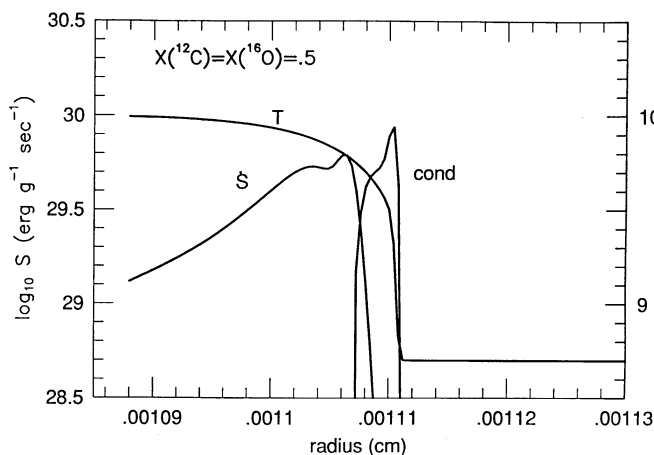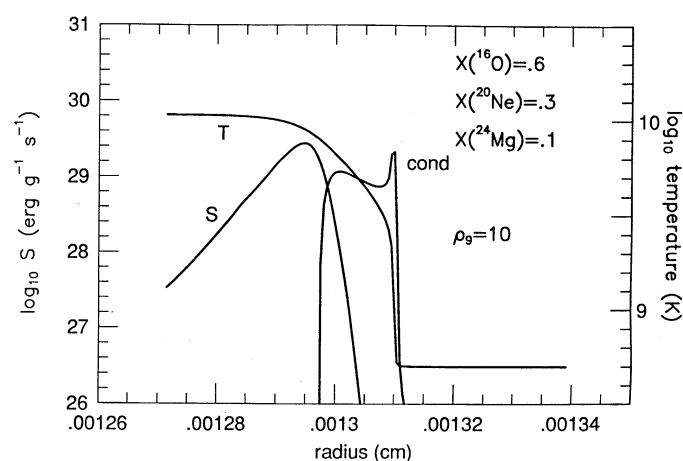

FIG. 3.—Magnitudes of the total nuclear generation rate, the energy conduction rate, and the temperature as a function of distance across the flame front for (a) a C+O mixture and (b) a O+Ne+Mg mixture. The flame is propagating to the right. The critical temperature T_{crit} is defined in the steady state when the energy generation within the flame equals the energy diffusion rate, here about 5×10^9 K. The sharp temperature gradient that occurs when energy is first diffused into a zone accounts for the spike in the energy conduction rate curve.
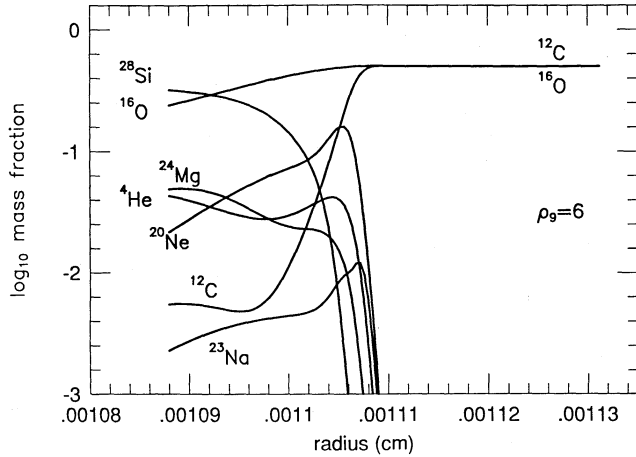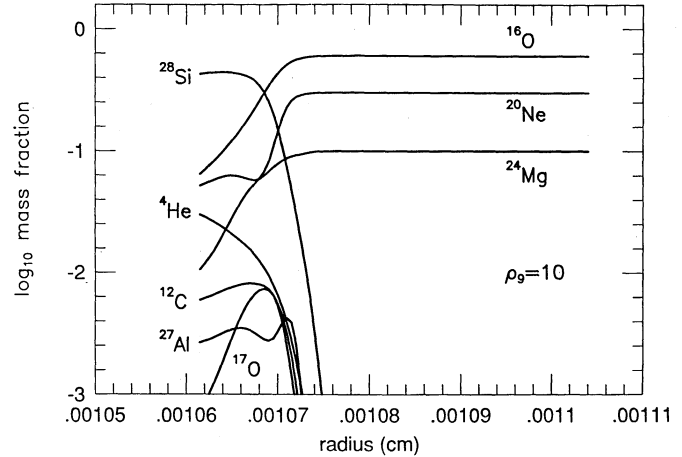
FIG. 4a

FIG. 4b

FIG. 4.—Composition in and behind steady state wave fronts in (a) C+O mixtures and (b) O+Ne+Mg mixtures as a function of distance. The flame is propagating to the right. The emission of α-particles by carbon and oxygen burning (initially) ensures energetic flows to the more tightly bound Si-peak nuclei.

The isotopic mass fractions as a function of distance are shown in Figure 4a for the standard C+O mixture and density. The corresponding plot for the standard O + Ne + Mg composition and density are shown in Figure 4b. As energy first diffuses into the cold C + O mixture, the dominant nuclear reaction is carbon burning. The resulting decay of the excited ^{24}Mg compound nucleus accounts for the initial increase in the ^{20}Ne, ^{23}Na, ^{23}Mg, n, p, and α-particle mass fractions. At the critical temperature the dominant flows of carbon burning are into ^{20}Ne via the reactions ^{23}Na$(p, \alpha)^{20}$Ne, ^{23}Mg$(n, p)^{23}$Na, and ^{23}Mg$(n, \alpha)^{20}$Ne. As the deflagration wave sweeps over and the temperature increases, there is a steady increase in the silicon group isotopes. Farther behind the flame front at about $T_9 \approx 8$, the temperature has increased to the point where endoergic photodisintegration reactions dominate and memory of the initial composition is erased as nuclear statistical equilibrium comes to exist.

Almost the same situation occurs in the O + Ne + Mg case, except that oxygen burning with the subsequent decay of the excited ^{32}S compound nucleus accounts for the rise in the ^{28}Si, ^{31}P, ^{31}S mass fractions. However, the preexistence of significant mass fractions of neon and magnesium means that this nuclear burning sequence produces less energy than the corresponding sequence in which neon and magnesium are initially absent (e.g., C+O material). Other factors being equal, the reduced nuclear generation rate is physically why O + Ne + Mg deflagrations are slower than C + O deflagrations.

The sensitivity of the flame speed to the nuclear reaction network itself was examined by using the five different networks discussed in § 2 and shown in Table 1. The results, given in Table 5, indicate that the use of a small network will underestimate the flame speed. The flattening of the flame speed with increasing number of isotopes is expected as the nuclear energy generation rate becomes well defined at a modest number of isotopes, presumably approaching the correct value asymptotically.

The physical properties of the flame are remarkably robust with respect to variation of several key nuclear reaction rates. With a large network the number of available reaction channels is large, so that variation in the efficiency of one channel is compensated for by others. This is not the case if a small

α-chain network is used. In that case, there is only one direction for the flow, and one might conclude (erroneously) that ^{20}Ne$(\alpha, \gamma)^{24}$Mg controlled the flame speed in C+O material. In particular, the effects of changing the reaction rates for ^{12}C + ^{12}C, ^{12}C + ^{16}O, ^{12}C$(\alpha, \gamma)^{16}$O, ^{16}O + ^{16}O, ^{20}Ne$(\alpha, p)^{23}$Na, ^{23}Na$(\alpha, p)^{26}$Mg, ^{23}Na$(p, n)^{23}$Mg, ^{20}Ne$(\alpha, \gamma)^{24}$Mg, and ^{24}Mg$(\alpha, p)^{27}$Al by factors of 1/10, 1/2, 2, and 10 with the 130 isotope network were investigated. Not surprisingly, the largest changes in the flame speed were due to variations in the carbon-burning rate for C+O dwarfs and the oxygen-burning rate for O + Ne + Mg dwarfs. The critical temperature, relevant mass fraction, and flame speed are shown in Table 6 for variations of certain key reaction rates. What is initially surprising is that the flame speed only increases marginally when the relevant reaction rate is increased by an order of magnitude.

For C + O dwarfs the energy generation rate in the vicinity of T_{crit} is $\dot{S} \sim X^2(^{12}\text{C})\lambda_{12,12} \sim X^2(^{12}\text{C})T_{\text{crit}}^{11.8}$, while the electron thermal opacity near the critical temperature is $\kappa \sim T_{\text{crit}}^{2.1}$. Thus from equation (4) one expects $v_{\text{cond}} \sim X(^{12}\text{C})T_{\text{crit}}^{4.85}$, where the carbon mass fraction is also evaluated at the critical temperature. Typically $X(^{12}\text{C})$ at T_{crit} is a few percent lower than the initial carbon mass fraction, and the roughly linear dependence of the flame speed on the initial carbon mass fraction is in accord with the exact calculations of Table 3. The primary response of equation (45) to increases in $\dot{S}$ is to increase the temperature gradient (i.e., the flame becomes thinner) and hence suppress the critical temperature only slightly. This implies a marginally faster flame speed (see Table 6). A similar

TABLE 5

FLAME SPEED (km s^{-1}) FOR DIFFERENT NUCLEAR REACTION NETWORKS

Number of Isotopes	O + Ne + Mg at $\rho_9 = 10$	C + O at $\rho_9 = 6$
9	54.4	113
19	71.9	172
32	79.1	188
83	87.2	211
130	87.5	214

TABLE 6

FLAME SPEEDS (km s^{-1}) FOR DIFFERENT NUCLEAR
REACTION RATES[a]

Rate	Factor	T_{crit}	X	v_{cond}
$\lambda_{12,12}$	0.1	6.735	0.4093	194
	0.25	6.027	0.4379	202
	1.0	5.256	0.4542	214
	4.0	4.608	0.4716	234
	10.0	4.253	0.4808	251
$\lambda_{p\alpha}(^{23}Na)$	0.1	5.257	0.4541	211
	0.25	5.256	0.4542	213
	1.0	5.256	0.4542	214
	4.0	5.254	0.4544	216
	10.0	5.255	0.4547	218
$\lambda_{16,16}$	0.1	8.790	0.5193	77.1
	0.25	7.879	0.5335	82.1
	1.0	7.120	0.5470	87.5
	4.0	6.377	0.5641	98.7
	10.0	5.910	0.5774	108

[a] The entries were computed with the 130 isotope network listed in Table 1. The first two reaction rates listed are for an initial composition of $X(^{12}C) = X(^{16}O) = 0.5$ at $\rho_9 = 6$. The mass-fraction entries X are the carbon mass fractions at the associated critical temperature. The last reaction rate is for an initial composition of $X(^{16}O) = 0.6$, $X(^{20}Ne) = 0.3$, and $X(^{24}Mg) = 0.1$ at $\rho_9 = 10$. In this case the mass-fraction entries are the oxygen mass fraction at the critical temperature. The reaction rate is in units of s^{-1} and T_{crit} is in T_9.

analysis holds for O+Ne+Mg dwarfs with $v_{cond} \sim X(^{12}C)T_{crit}^{5.12}$. Variations in the other reaction rates listed above gave no significant changes to the properties of the deflagration wave. In these studies both the forward and reverse rates were varied by the same factor to preserve detailed balance.

Figure 5 shows the dependence of T_{crit} in the ρ-T plane when $X(^{12}C) = X(^{16}O) = 0.5$. The solid line indicates where the

photon opacity is equal to the conductive opacity. Areas below the solid line have flamed dynamics that are dominated by the electron thermal conductivity, while regions above the solid line are radiation-dominated processes. The shaded polygon is the operating region of the deflagration waves. Except for the very lowest densities considered, the critical temperature of the flame is in the regime where the thermal conductivity of the relativistic, degenerate electrons controls the flame properties.

The response of the flame speed to variations in the thermal conductivity for the standard C+O and O+Ne+Mg mixtures is shown in Table 7. Scaling relations between the flame speed and the conductivity are predicted rather well by the order-of-magnitude estimate given in equation (4). The flame speed is much more sensitive to the conductivity than to the nuclear reaction rates, the former dictating the rate at which energy can be transported. Also shown in Table 7 are the flame speeds obtained if $P\,dV$ work terms in the energy equation are absent (and the conductivity is at its nominative value). As explained in § 2, the overestimation of the flame speed by about 40% is due to not allowing a zone to expand. This artificially increases the critical temperature and hence the flame speed.

3.3. The Trigger Mass

From equation (3) one may estimate the minimum amount of mass, the "trigger mass," necessary to ignite a stable conductive wave front:

$$M_{trig} \approx \frac{4}{3}\pi\delta^3\rho \approx \frac{4}{3}\pi\rho\left(\frac{\lambda cE}{\dot{S}}\right)^{3/2}, \quad (46)$$

which is strongly dependent on the temperature via $\dot{S}$ and E. The trigger mass as a function of temperature is shown in Figure 6 for C+O and O+Ne+Mg compositions over a range of unburned densities. The critical temperature T_{crit} is represented by the vertical dashed line and is marked on the temperature axis of Figure 6. The trigger mass curves delineate
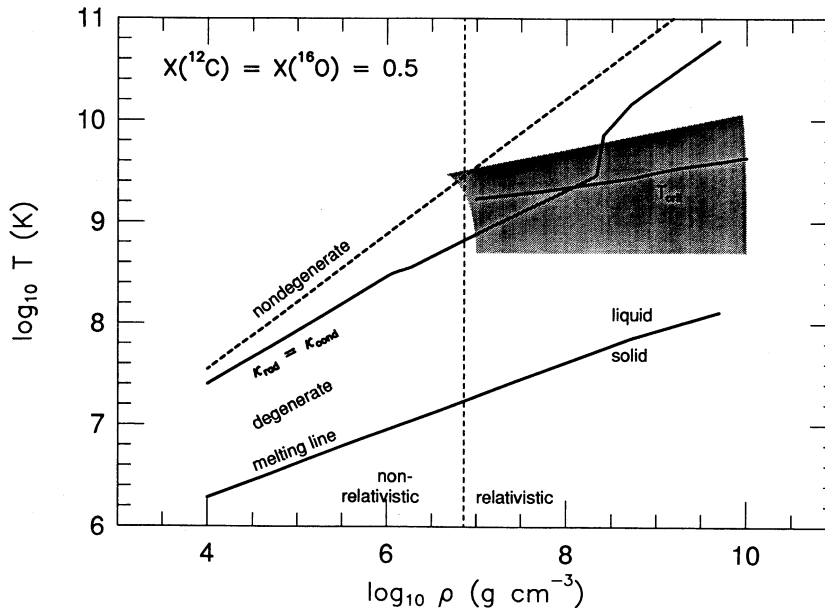

FIG. 5.—The ρ-T plane for $X(^{12}C) = X(^{16}O) = 0.5$. Above the solid line marked $\kappa_{rad} = \kappa_{cond}$, heat is transported primarily by radiative diffusion; below the line it is transported by thermal conduction. The boundaries between the various relativistic and degenerate regimes are indicated by the dashed lines. Below the melting line the ions crystalize. The shaded polygon is the region where deflagration waves operate, with the critical temperature of the flame delineated by the solid line.

TABLE 7

FLAME SPEEDS (km s^{-1}) FOR DIFFERENT THERMAL CONDUCTIVITIES

Composition	ρ_9	$\sigma \times 1$	$\sigma \times 2$	$\sigma \times 0.5$	Zero $P\,dV$ Work
$X(^{12}C) = 0.5, X(^{16}O) = 0.5$	10.0	307	421	237	542
	8.0	256	354	195	467
	6.0	214	288	164	401
	4.0	143	291	115	262
	2.0	75.8	98.7	56.6	140
	1.0	36.4	46.4	29.7	68.8
	0.5	18.1	21.6	14.7	34.3
	0.2	6.15	7.69	5.34	11.1
$X(^{16}O) = 0.6, X(^{20}Ne) = 0.3$	14.0	121	151	95.6	221
	12.0	104	127	83.5	185
	10.0	87.5	110	66.7	162
	8.0	69.6	88.4	73.2	121
	6.0	51.9	67.4	52.2	92.8
	4.0	33.6	44.5	24.8	54.1
	2.0	18.2	23.7	12.9	28.8
	1.0	6.36	8.19	4.99	10.4

two regions. The region below the curve corresponds to cases where the energy input to the given mass is unable to raise the temperature to the critical temperature T_{crit}. The disturbance will simply diffuse away, returning to the ambient temperature, since the diffusion time scale is much shorter than the burning time scale. The area above the curve corresponds to over driven cases, where the energy input is enough (or more than enough) to achieve the critical temperature T_{crit} and thus propagate a steady state wave. This is the case where the burning time scale is at least as quick as the diffusion time scale, and in fact much quicker. A trigger energy may be defined as

$$E_{trig} = (T - T_{cold}) \frac{\partial E}{\partial T} M_{trig} \qquad (47)$$

and is shown as the right-hand axis in Figure 6. The trigger

FIG. 6.—Trigger mass as a function of the perturbing temperature and density for C + O and O + Ne + Mg compositions. The critical temperature T_{crit}, where the nuclear energy generation rate is equal to the energy conduction rate, is marked by the dashed line. Initial conditions below the trigger mass curves, indicated by the crossed circle, cannot sustain a steady state wave and simply cool off on diffusive time scales. The general direction of the evolution is indicated by the arrows. Conditions initially above the curves can propagate deflagration waves. The schematic evolution of several mass points is indicated. The trigger energy, related to the trigger mass by eq. (47), is shown on the right-hand axis.

energy curves represent the energy input necessary to propagate a steady state deflagration wave.

Several initial starting temperatures of various masses are shown in Figure 6 as the crossed circles. The subsequent evolution is shown schematically by the solid arrows. Points below the critical mass curve, as expected, give an energy that diffuses away. Points at the upper right correspond to a very over-driven disturbance, where the initial perturbing temperature is much greater than the final burn temperature of the mass point. In this case the temperature is quickly reduced by photodisintegration and neutrino losses. A point starting at the upper left, although it has less energy, is capable (because of its much larger mass) of raising the temperature past the critical temperature by burning. The region in Figure 6 having a higher temperature than the critical temperature T_{crit} was investigated using the diffusion code to assess the validity of using the order-of-magnitude estimate relations. The actual trigger mass, as determined from the diffusion code, is in the worst case a factor of 2 different from what the order-of-magnitude relations in equation (46) would predict.

3.4. Symmetry and the Hugoniot Jump Relations

In the case of a deflagration which begins at the origin in a spherically symmetric system, the material velocity behind the front must eventually become zero in order to satisfy the boundary condition at the origin. In addition, deflagrations must obey a Hugoniot jump condition (Courant & Friedrichs 1948). The only way in which these two conditions can both be satisfied is if the deflagration is preceded by a compression wave that accelerates the material away from the subsonic burning front. Subsequent passage of the deflagration front will then provide exactly the correct jump in the material velocity so that the material behind the front will come to rest. This is physically possible, since the deflagration is subsonic. Figure 7 shows, for both a C + O mixture and an O + Ne + Mg mixture, the material velocity v, as computed by KEPLER, obeying both the zero-velocity boundary condition at the origin and a Hugoniot jump condition at the burning front interface. The nonzero material velocity of the material ahead of the flame interface is due to the previous passage (not shown in the figure) of a compression wave. The jump velocity is larger in C + O dwarfs than in O + Ne + Mg dwarfs because C + O mixtures have a higher flame speed.
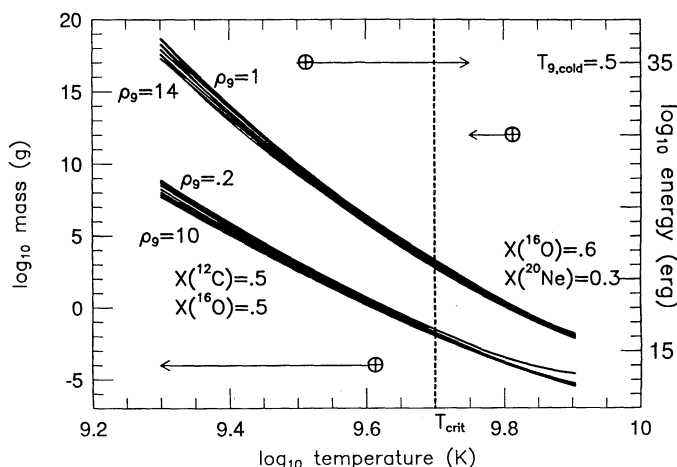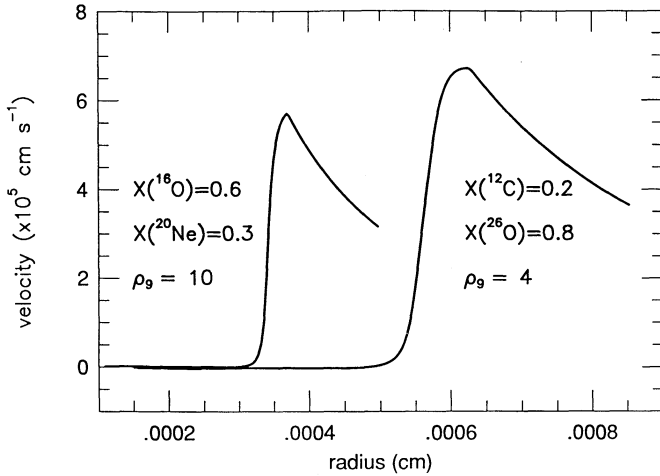
FIG. 7.—Velocity profile in and behind the deflagration wave. Ahead of the wave front a compression wave has accelerated material away from the deflagration front. When the deflagration wave passes through this material, the Hugoniot jump in the velocity is such that the zero-velocity boundary condition is satisfied.

4. STABILITY AND ACCELERATION OF THE FLAME BY THE RAYLEIGH-TAYLOR INSTABILITY

As the laminar conductive wave travels radially outward in the white dwarf, the temperature behind the wave front increases, the composition is burned into nuclear statistical equilibrium, the density behind the flame front decreases, and the absolute strength of the gravitational field increases. The crossed gravitational and density gradients cause a Rayleigh-Taylor (RT) instability to develop. The dispersion relation for the RT instability, assuming infinitely deep fluid layers and derived from normal mode analysis of the linearized fluid equations (Rayleigh 1893; Taylor 1950; Chandrasekhar 1961) is

$$\omega^2 = gk \frac{(\rho_2 - \rho_1)}{(\rho_2 + \rho_1)} = gk \frac{\Delta\rho}{2\bar{\rho}} , \qquad (48)$$

or, in terms of wavelength ($k = 2\pi/\lambda$) and period ($\omega = 2\pi/T$),

$$T^2 = 4\pi\lambda \left(g \frac{\Delta\rho}{\bar{\rho}} \right)^{-1} . \qquad (49)$$

Strictly speaking, it is not possible to define a period for the RT instability, since the motion is not periodic. Nevertheless, for simplicity, we refer to $T = 2\pi/\omega$ as the "period" or "growth rate" of the RT instability. This definition of the period is consistent with the use of Fourier normal mode analysis and is similar to the definition of period for damped harmonic oscillations (Marion 1970; Goldstein 1980). Adopting an alternative definition of $1/\omega$ for the growth rate may not be consistent with the use of normal mode perturbation analysis. In either case, the normal conductive propagation speed inhibits the growth of small length scale deformations, so that the minimum length scale $\lambda_{\min}$ that can begin to deform the laminar wave front follows equation (48) and

$$v_{\mathrm{cond}} T(\lambda_{\min}) = \lambda_{\min} , \qquad (50)$$

that is,

$$\lambda_{\min} = 4\pi v_{\mathrm{cond}}^2 \left(g \frac{\Delta\rho}{\bar{\rho}} \right)^{-1} . \qquad (51)$$

Assuming

$$M \approx \tfrac{4}{3}\pi\rho r^3 , \qquad (52)$$

it follows that equation (51) may be expressed as

$$\lambda_{\min} \approx 3 v_{\mathrm{cond}}^2 \left(Gr\rho \frac{\Delta\rho}{\bar{\rho}} \right)^{-1} . \qquad (53)$$

As the flame propagates radially outward, the minimum length scale for turbulent motion becomes smaller as the acceleration becomes larger.

At densities appropriate to C+O and O+Ne+Mg white dwarfs, electron capture in an isobaric nuclear statistical equilibrium environment causes the number of electrons per baryon, $Y_e = (n_e/\rho N_A)$, to decrease and the density to increase behind the flame. The temporal evolution of the density for an initial O+Ne+Mg composition is shown in Figure 8. The dashed lines represent the initial density, while the solid lines represent the density evolution. The intersection of these two curves defines a "recovery time," t_{recov}, for the density to return to its value ahead of the flame. In order to follow the evolution of Y_e, it was necessary to use a larger nuclear reaction network. Consequently, following oxygen depletion of the burning material, we switched to a 125 isotope nuclear reaction network in the hydrodynamical code to follow the nucleosynthesis. The rates and network have been discussed by WZW and by Weaver, Woosley, & Fuller (1984).

The fact that the density recovers its initial value implies the existence of a maximum spatial extent of density inversion. This in turn suggests the existence of a maximum deformation length scale $\lambda_{\max}$,

$$\lambda_{\max} = v_{\mathrm{cond}} t_{\mathrm{recov}} . \qquad (54)$$

Equation (54) is very simple and has its limitations. The referee correctly pointed out that in a turbulent flow the recovery time may be changed from its laminar flow value. In addition, the effective flame speed should replace the conductive speed
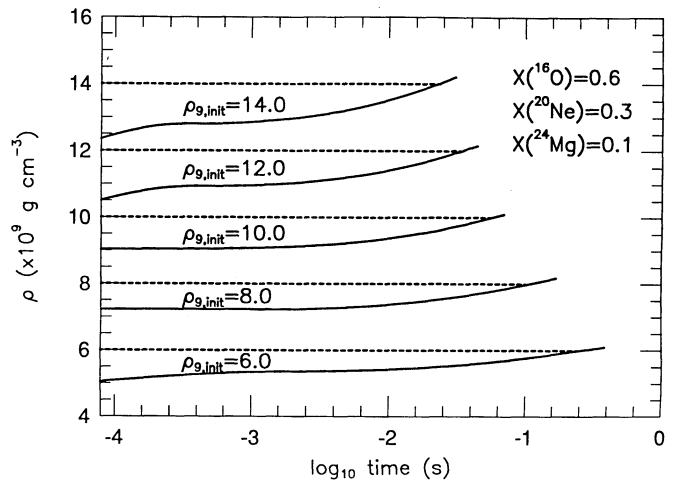

FIG. 8.—Temporal evolution of the density behind the deflagration front in an isobaric nuclear statistical equilibrium environment for an O+Ne+Mg composition. The intersection of the dashed lines, which represent the initial density, and the solid lines, which represent the density evolution, defines the recovery time t_{recov}. The increase in density is due to electron capture, which also decreases Y_e. The recovery time multiplied by the conductive speed gives the thickness of the density inversion layer, which is also the maximum Rayleigh-Taylor unstable wavelength that can form.

for turbulent, chaotic flows. These considerations, worth pursuing in future studies, do not change the idea that there is a maximum thickness to the density inversion, hence a maximum unstable wavelength. Small changes to λ_{max} should not significantly change the major conclusions of this paper.

Equation (48) states that there is no intrinsic upper bound to the wavelengths susceptible to RT deformation of two infinitely thick fluids. As shown in Figure 8, the density rebounds to its initial density. The density inversion has a finite thickness. The dispersion relation, assuming linearized fluid equations and normal mode analysis, for a layer of finite thickness is a quartic in ω (Taylor 1950). The essential point, gained by the complication of adding a layer, is that the thickness of the layer establishes a maximum on the unstable wavelengths. Indeed, in the limit of the layer becoming infinitely thick, the dispersion relation simplifies to equation (48), where all wavelengths are unstable, while in the opposite limit of a vanishing layer thickness there is no RT instability at all! This limit of vanishing layer thickness touches on an important point for regions of intermediate thickness, namely, that wavelengths much larger than the thickness of the layer do not detect crossed gravitational and density gradients and therefore are not subject to Rayleigh-Taylor instability. This behavior was still present even in the nonlinear regime of the RT instability investigated by Vernon et al. (1982).

The width of the density inversion behind the subsonic conduction front, λ_{max}, and the minimum instability wavelength λ_{min} per 100 km (of burned material), are shown as a function of the initial density for three different C+O compositions in Figure 9a and for three different O+Ne+Mg compositions in Figure 9b. At initial C+O densities above about $\rho_9 = 6$ and initial O+Ne+Mg densities above about $\rho_9 = 10$, with a fairly strong dependence on composition, the maximum length scale of deformation λ_{max} that can grow begins to be smaller than the minimum length scale λ_{min}. This implies that the conductive flame will remain stable. This case corresponds to an undeformed surface, a plane whose fractal dimension is, by definition, $D = 2$. The flame speed remains at its conductive value, and the analysis in § 2 is applicable.

The conductive flame speed retains its significance as the speed of the flame only if the mechanism of propagation does not change because of turbulence or the formation of detonation waves. If, for example, the thickness of the front is large compared with the smaller unstable wavelengths, then the front will become a wrinkled, deformation, and perhaps even disconnected surface characterized by a range of deformations from λ_{min} to λ_{max}. In this case the velocity of the front is increased compared with the conductively propagated deflagration, primarily because of an increase in the surface area of the front and subsequently by an increase in the fractal dimension. Woosley (1990) showed that one may treat the expanding area of the turbulent burning region as a fractal whose tile size is identical to the minimum unstable RT wavelength λ_{min}. This choice ensures that the prerequisite Mandelbrot (1983) scaling relation between area and volume is preserved. Woosley (1990) further demonstrated that the effective turbulent velocity v_{eff} is given by

$$v_{eff} = v_{cond}\left(\frac{\lambda_{max}}{\lambda_{min}}\right)^{D-2},\qquad(55)$$

where D is the fractal dimension. The effective velocity flame speed as a function of distance, density, and fractal dimension for the standard C+O composition is shown in Figure 10a, while Figure 10b shows the corresponding situation for the standard O+Ne+Mg composition.

Various calculations (Nomoto & Kondo 1991; Canal et al. 1990a; Isern et al. 1991) have shown a bifurcation between collapse and explosion of the white dwarf at ratios of the effective flame speed to the sound speed around 3% (larger in the study by Isern et al.). Figures 8 and 9 indicate that for all reasonable values of the fractal dimension, for initial C+O or O+Ne+Mg densities above 9×10^9 g cm^{-3} the white dwarf probably collapses to a neutron star. While the fractal dimension $2 \lesssim D \lesssim 3$ remains a free parameter, and is quite likely itself a function of distance, the physical conditions that lead to accretion-induced collapse of white dwarfs are apparently not particularly sensitive to the choice of the fractal dimension,
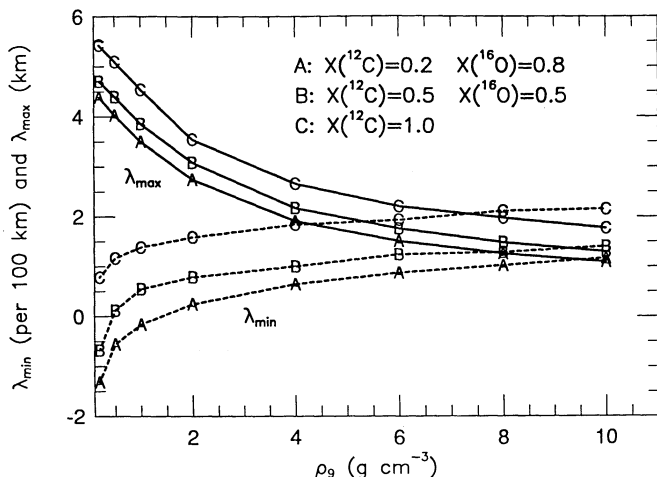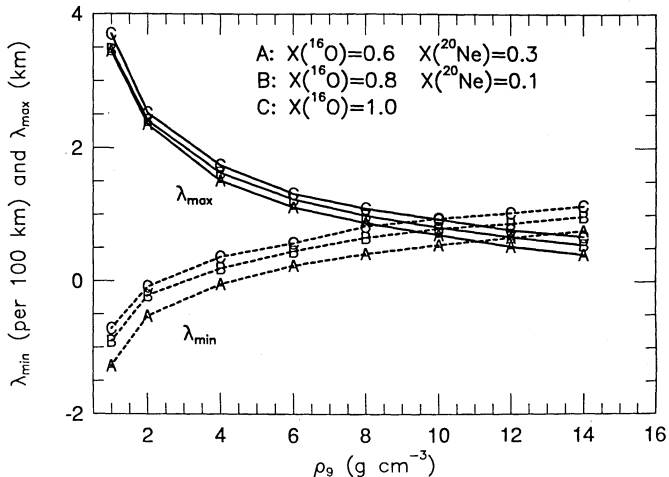

FIG. 9a

FIG. 9b

FIG. 9.—Thickness of the density inversion behind the subsonic conduction front, λ_{max}, and the minimum wavelength instability λ_{min} per 100 km as a function of the initial density for various (a) C+O and (b) O+Ne+Mg mixtures. Flames propagating in white dwarfs that have initial densities such that the minimum unstable length scale is greater than the thickness of the density inversion will remain stable. The white dwarf will probably collapse to a neutron star.
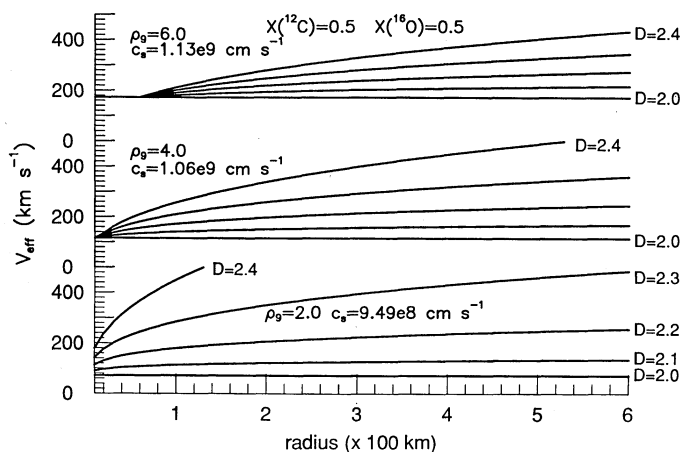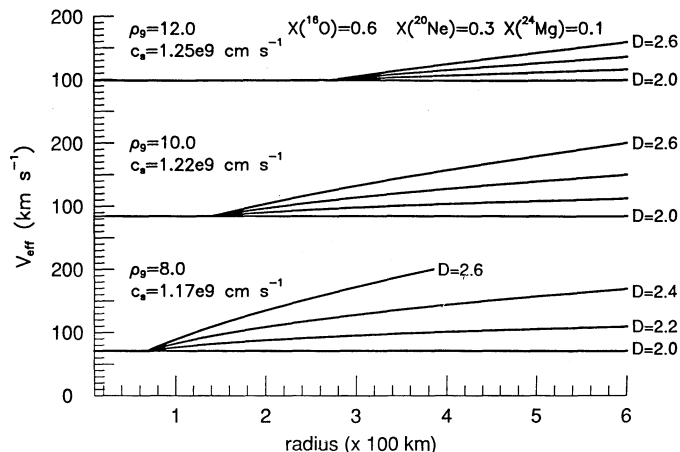
FIG. 10a

FIG. 10b

FIG. 10.—Effective velocity as a function of the average radius of burned material for (a) C+O ignition densities of $\rho_9 = 2$, $\rho_9 = 4$, and $\rho_9 = 6$ and (b) for O+Ne+Mg ignition densities of $\rho_9 = 8$, $\rho_9 = 10$, and $\rho_9 = 12$. The effective speed of the flame is dependent on the value of the fractal dimension D, taken here to be a strict constant for all densities. Prior to the point where $\lambda_{max} = \lambda_{min}$, $D \equiv 2$.

given the small range between λ_{min} and λ_{max}. Also, one does not expect values for D greater than about 2.7; values of 2.6 commonly typify fully developed turbulence or a highly convoluted surface (Mandelbrot 1983 and references therein). In addition, using the flame speeds presented in this paper, we have completed several KEPLER simulations of AIC that confirm the above bifurcation point between collapse and explosion.

Finally, we consider the possibility that, in the O+Ne+Mg case, electron capture prior to the point where the runaway becomes localized may have led to a significant change in composition so that neutron-proton equality no longer prevails. Y_e in the center of the white dwarf when it runs away may be as low as 0.48 (K. Nomoto 1991, private communication). Also, in the C+O case Population I white dwarfs will have $Y_e \approx 0.498$. We examined the flame speed for these two initial Y_e conditions with a 130 isotope network using ^{22}Ne instead of ^{20}Ne to lower Y_e from its fiducial value of 0.5. Over the range of densities considered in this work, the flame speed decreased at most by about 30% in the O+Ne+Mg case and by about 5% in the C+O case. In addition, we investigated the effect of a lower initial value of Y_e on the density recovery time. No significant differences were found as compared with material with an initial $Y_e = 0.5$. The tentative conclusion is that a lower initial value of Y_e will not affect the results of the previous discussion in a substantial fashion, at least so long as $Y_e \gtrsim 0.48$.

5. CONCLUSIONS

We have calculated the physical properties of conductive, isobaric, subsonic flames for a variety of compositions under degenerate conditions. Remarkably consistent properties were found using four independent methods of computation: micro-zoned hydrodynamics, energy diffusion, energy eigenvalue equations, and an integral approach developed by Zel'dovich et al. (1985). Summary formulae for the flame speed as a function of density and composition are given for C+O material in equation (43) and for O+Ne+Mg in equation (44). The exact flame speeds and many other physical properties of the flame front are given in Tables 3 and 4. The critical temperature T_{crit}, where the exothermic nuclear energy generation rate is equal

to the conduction energy diffusion rate, was found to be near 5×10^9 K, with slight variations for different compositions and initial densities.

The flame speed is very robust with respect to variation of the nuclear reaction rates (owing to the large number of reaction channels available), but flame speeds computed with small networks (α-chain) yield results that underestimate the flame speed by about 50%, while calculations that ignore the $P\,dV$ work terms in the energy equation were shown to yield flame speeds that overestimate the flame speed by about 40%. The simple order-of-magnitude estimate given in equation (4) successfully predicts the proper scaling relationship with respect to variations in the initial carbon mass fraction, the nuclear reaction rates, and the thermal conductivity. With the flame speeds almost independent of variations in the nuclear reaction rates and the thermal conductivity being theoretically uncertain to about 20%, the physical properties of C+O and O+Ne+Mg deflagrations given in Tables 3 and 4 should be correct to about 10%.

The time scales for diffusion and nuclear burning were examined in the mass versus temperature diagram of Figure 6. Minimum trigger masses, for a given temperature perturbation, are shown and are defined by the boundary between material that could propagate a steady state, isobaric deflagration wave and material whose initial disturbance would simply thermally diffuse to the ambient temperature. Characteristic motion of initial perturbations in the mass-temperature diagram was discussed with respect to the critical temperature T_{crit} of the flame.

Electron capture in an isobaric nuclear statistical equilibrium environment causes the density to increase behind the deflagration wave front (see Fig. 8). There thus exists a maximum length scale of Rayleigh-Taylor instability formation. Treating the expanding area of the turbulent burning region as a fractal whose measurement scale is identical to the minimum length scale of Rayleigh-Taylor instability, we found, for all reasonable values of the fractal dimension, that for initial C+O or O+Ne+Mg white dwarf densities above 8×10^9 g cm^{-3} the white dwarf probably collapses to a neutron star.

APPENDIX

INTEGRATION OF NUCLEAR REACTION NETWORKS AS A SYSTEM OF ORDINARY DIFFERENTIAL EQUATIONS

Written as a set of ordinary differential equations (ODEs), the nuclear reaction equations

$$\dot{y} = f(y) \tag{A1}$$

are nonlinear and stiff, and possess right-hand sides that are independent of the integration variable. One approach in integrating a stiff system is the use of an implicit, first-order Euler method, which advances the system over a time step h according to

$$(1 - h\tilde{J}) \cdot y_{n+1} = y_n + hf(y_n) - h\tilde{J}y_n , \tag{A2}$$

where $\tilde{J}$ is the Jacobian of the nuclear reaction equations. Equation (A2) can be simplified, with the resulting numerical operation count decreased considerably, by solving for the change in y, $\Delta y = y_{n+1} - y_n$, instead of y itself. Being first-order accurate, equation (A2) furnishes no estimate of the local truncation error. This is a drawback, as automatic step-size adjustment based on the accuracy of an integration step cannot occur.

Another approach is the Kaps-Rentrop (1979) algorithm, in essence an implicit Runge-Kutta method. Their algorithm is fourth-order accurate and provides an estimate of the local truncation error. The added computational labor of these improvements (as compared with the Euler method) is small. There are only three additional back-substitution steps and assorted minor algebra to perform. The system is advanced in time according to

$$y_{n+1} = y_n + \sum_{i=1}^{4} c_i k_i , \tag{A3}$$

where the corrections k_i $(i = 1, 2, 3, 4)$ are found by solving the set of four linear equations

$$(1 - \gamma h\tilde{J}) \cdot k_i = hf\left(y_n + \sum_{j=1}^{i-1} \alpha_{ij} k_i\right) + h\tilde{J} \sum_{j=1}^{i-1} \gamma_{ij} k_j , \tag{A4}$$

where γ, γ_{ij}, c_i, and α_{ij} are given constants. A working version of this algorithm has been implemented by Press & Teukolsky (1989). All of the physical properties quoted in this paper were obtained with the fourth-order method.

The Jacobian matrix used in solving the stiff ODEs has the basic form of a doubly bordered band diagonal or "arrowhead" matrix (Tewarson 1973) and is shown in Figure 11 for the 130 isotope network given in Table 1. There are some off-band elements
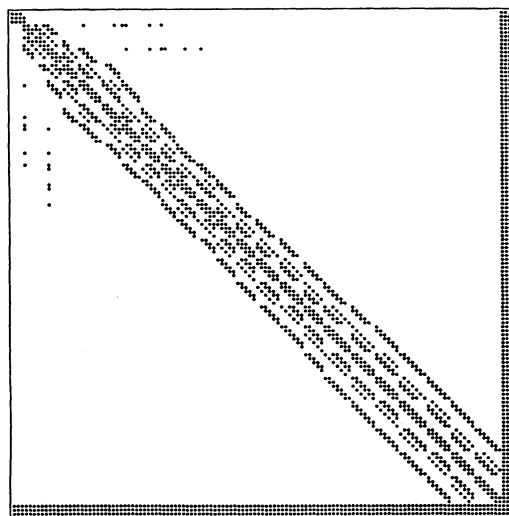

FIG. 11.—Structure of the Jacobian matrix used in integrating the nuclear reaction network as a system of ODEs. The Jacobian shown is for the 130 isotope network used to obtain the physical properties of the deflagration wave. The $J(1, 1)$ matrix element is in the upper left-hand corner, while $J(130, 130)$ is at the lower right.

due to low-Z isotopes and the heavy-ion reactions. The dense diagonal portion of the Jacobian has a bandwidth of 14, corresponding to the 14 different reaction paths $(n, \alpha), (\alpha, n), \ldots$, etc. The characteristic arrowhead formation is obtained by setting the neutron, proton, and α-particle ODEs to be the last three ODEs. The Jacobian matrix for this 130 isotope network is quite sparse, with only about 15% of its entries being nonzero.

We investigated four different techniques for solving the system of linear equations: (1) standard LU decomposition, (2) an iterative conjugate gradient method (Press et al. 1986), (3) Gaussian elimination that assumed diagonal dominance of the matrix (which is the case for nuclear reaction networks) and took advantage of zeros during the elimination stage, and (4) a direct sparse matrix LU decomposition (Pissanetsky 1984; Duff, Erisman, & Reid 1986; Eisenstat et al. 1982). Our test problem was to evolve an initial O + Ne + Mg composition into the steady state with 2000 time steps. A 103 element network was used in every zone (an average of about 60 zones with the moving mesh code). To compare all four methods fairly, the Euler method was chosen as the method of integration. The total CPU time, on one processor of a Silicon Graphics 240D computer, was 933 minutes for technique 1, 288 minutes for technique 2, 344 minutes for technique 3, and 162 minutes for technique 4. Using the fourth-order method and the direct sparse matrix solver consumed a total of 187 CPU minutes. The differences between the solution vectors as given by methods 1, 3, and 4 were of the order of machine precision. The iterative conjugate gradient method generated small negative mass fractions, something that was not seen in the other three methods. In addition to the CPU compression factors, the sparse matrix techniques required about 70% less computer storage. We conclude that the fourth-order accurate ODE solver combined with sparse matrix technology minimizes use of computer resources while balancing ease of use and accuracy.

REFERENCES

Alecian, G., & Vauclair, S. 1983, Fund. Cosmic Phys., 8, 369
Bailyn, C. D., & Grindlay, J. E. 1990, ApJ, 353, 159
Baron, E., Cooperstein, J., Kahana, S., & Nomoto, K. 1987, ApJ, 320, 304
Buchler, J. R., Colgate, S. A., & Mazurek, T. J. 1979, J. Phys., C2, 159
Buchler, J. R., & Yueh, W. R. 1976, ApJ, 210, 440
Burgers, J. M. 1969, Flow Equations for Composite Gases (New York: Academic)
Canal, R., Garcia, D., Isern, J., & Labay, J. 1990a, ApJ, 356, L51
Canal, R., Isern, J., & Labay, J. 1980, ApJ, 241, L33
———. 1990b, in ARA&A, Vol. 28, ed. G. Burbidge (Palo Alto: Annual Reviews), 183
Canuto, V. 1970, ApJ, 159, 641
Caughlan, G. R., & Fowler, W. A. 1988, Atomic Data Nucl. Data Tables, 40, 283
Chandrasekhar, S. 1961, Hydrodynamic and Hydromagnetic Stability (Oxford: Oxford Univ. Press)
Chapman, S., & Cowling, T. G. 1970, The Mathematical Theory of Non-uniform Gases (Cambridge: Cambridge Univ. Press)
Chin, C. 1965, ApJ, 142, 1481
Chiu, H. Y. 1968, Stellar Physics (Waltham: Blaisdell)
Clayton, D. D. 1968, Principles of Stellar Evolution and Nucleosynthesis (Chicago: Univ. Chicago Press)
Cloutman, R. A. 1990, ApJS, 71, 677
Courant, R., & Friedrichs, K. O. 1948, Supersonic Flow and Shock Waves (New York: Wiley)
Cox, L. P., & Giuli, R. T. 1968, Principles of Stellar Structure (New York: Gordon & Breach)
Crank, J., & Nicolson, P. 1947, Proc. Cambridge Phil. Soc., 43, 50
Divine, T. N. 1965, ApJ, 142, 1652
Duff, I. S., Erisman, A. M., & Reid, J. K. 1986, Direct Methods for Sparse Matrices (Oxford: Oxford Univ. Press)
Eisenstat, S. C., Gursky, M. C., Schultz, M. H., & Sherman, A. H. 1982, Yale Sparse Matrix Package (Yale Department of Computer Science Rep., No. 114)
Flowers, E., & Itoh, N. 1976, ApJ, 206, 218
Fowler, W. A., & Vogl, J. L. 1964, Lectures in Theoretical Physics (Boulder: Univ. Colorado Press)
Frank-Kamenetskii, D. A. 1969, Diffusion and Heat Transfer in Chemical Kinetics (New York: Plenum)
Fryxell, B. A., & Woosley, S. E. 1982, ApJ, 261, 332
Garcia, D., Labay, J., Canal, R., & Isern, J. 1991, preprint
Goldstein, H. 1980, Classical Mechanics (Menlo Park: Addison-Wesley)
Goodman, J. 1986, ApJ, 308, L47
Goodman, J., Dar, A., & Nussinov, S. 1987, ApJ, 314, L51
Hachisu, I., Eriguchi, Y., & Nomoto, K. 1986a, ApJ, 308, 161
———. 1986b, ApJ, 311, 214
Hubbard, W. B. 1966, ApJ, 146, 858
Hubbard, W. B., & Lampe, M. 1969, ApJS, 18, 279
Iben, I., Jr., Fujimoto, M. Y., & MacDonald, J. 1991, ApJ, 375, L27
Iben, I., Jr., & MacDonald, J. 1985, ApJ, 296, 540
Isern, J., Canal, R., & Labay, J. 1991, preprint
Isern, J., Labay, J., Hernanz, M., & Canal, R. 1983, ApJ, 273, 320
Itoh, N., Kojo, K., & Nakagawa, M. 1990, ApJS, 74, 291
Itoh, N., Mitake, S., Iyetomi, H., & Ichimaru, S. 1983, ApJ, 273, 774
Kaps, P., & Rentrop, P. 1979, Numer. Math., 33, 55
Kawai, Y., Saio, H., & Nomoto, K. 1987, ApJ, 315, 229
Kuo, K. K. 1986, Principles of Combustion (New York: Wiley)
Landau, L. D., & Lifshitz, E. M. 1959, Course in Theoretical Physics, Vol. 6, Fluid Mechanics (Oxford: Pergamon)
Lee, T. D. 1950, ApJ, 111, 625

Livio, M., & Truran, J. W. 1991a, preprint
———. 1991b, preprint
Mandelbrot, B. B. 1983, The Fractal Geometry of Nature (New York: Freeman)
Marion, J. B. 1970, Classical Dynamics of Particles and Systems (San Francisco: Academic)
Mayle, R. W., & Wilson, J. R. 1988, ApJ, 334, 909
Miyaji, S., & Nomoto, K. 1987, ApJ, 318, 307
Miyaji, S., Nomoto, K., Yokoi, K., & Sugimoto, D. 1980, PASJ, 32, 303
Munakata, H., Koyama, Y., & Itoh, N. 1985, ApJ, 296, 197; 304, 580 (1986)
Nandkumar, R., & Pethick, C. J. 1984, MNRAS, 209, 511
Nomoto, K. 1986, Prog. Part. Nucl. Phys., 17, 249
Nomoto, K., & Iben, I. 1985, ApJ, 297, 531
Nomoto, K., & Kondo, Y. 1991, ApJ, 367, L19
Nomoto, K., Miyaji, S., Sugimoto, D., & Yokoi, K. 1979, in IAU Colloq. 53, White Dwarfs and Variable Degenerate Stars, ed. H. M. Van Horn & W. Weidemann (Rochester: Rochester Univ. Press), 56
Nomoto, K., Thielemann, F. K., & Yokoi, K. 1984, ApJ, 286, 644
Paczyński, B. 1986, ApJ, 308, L43
———. 1990, ApJ, 363, 218
Paquette, C., Pelletier, C., Fontaine, G., & Michaud, G. 1986, ApJS, 61, 177
Pissanetsky, S. 1984, Sparse Matrix Technology (New York: Academic)
Pollock, E., & Hansen, J. 1973, Phys. Rev. A, 8, 3110
Press, W. H., Flannery, B. P., Teukolsky, S. A., & Vetterling, W. T. 1986, Numerical Recipes: The Art of Scientific Computing (Cambridge: Cambridge Univ. Press)
Press, W. H., & Teukolsky, S. A. 1989, Comput. Phys., 88, 2
Raikh, M. E., & Yakovlev, D. G. 1982, Ap&SS, 87, 193
Ramaty, R., & Dar, A. 1990, preprint
Ramos, J. I. 1987, in Numerical Fluid Mechanics and Heat Transfer, ed. T. C. Chawla (New York: Hemisphere), 150
Rayleigh, L. 1893, Proc. Lond. Math. Soc., 14, 170
Saio, H., & Nomoto, K. 1985, A&A, 150, L21
Salpeter, E. 1957, ApJ, 134, 669
Sampson, D. H. 1959, ApJ, 129, 734
Schwarzschild, M., & Härm, R. 1965, ApJ, 142, 855
Shemi, A., & Piran, T. 1990, ApJ, 365, L55
Taylor, G. 1950, Proc. R. Soc. London, A, 201, 192
Tewarson, R. P. 1973, Sparse Matrices (New York: Academic)
Timmes, F. X. 1990, private communication
———. 1992, ApJ, 390, L107
Urpin, V. A., & Yakovlev, D. G. 1980, Soviet Astron., 24, 126
Vernon, C. P., McCrory, R. L., Morse, R. L., Baker, G. R., Meiron, D. I., & Orszag, S. A. 1982, Phys. Fluids, 25, 1653
van den Heuvel, E. P. J. 1984, J. Astrophys. Astron., 5, 209
———. 1987, in IAU Symp. 125, The Origin and Evolution of Neutron Stars, ed. D. Helfand & J. Huang (Dordrecht: Reidel), 393
Wallace, R. K., Woosley, S. E., & Weaver, T. A. 1982, ApJ, 258, 696
Weaver, T. A., Woosley, S. E., & Fuller, G. M. 1984, in Numerical Astrophysics, ed. J. Centrella, J. LeBlanc, & R. Bowers (Boston: Jones & Bartlett), 374
Weaver, T. A., Zimmerman, G. B., & Woosley, S. E. 1978, ApJ, 225, 1021 (WZW)
Williams, F. A. 1988, Combustion Theory (Menlo Park: Benjamin-Cummings)
Woosley, S. E. 1986, in Nucleosynthesis and Chemical Evolution, ed. B. Hauck, A. Maeder, & G. Meynet (Geneva: Swiss Society of Astrophysics and Astronomy, Geneva Observatory), 1
———. 1990, in Supernovae, ed. A. G. Petschek (New York: Springer-Verlag), 182
Woosley, S. E., & Baron, E. 1992, ApJ, 391, 228

Woosley, S. E., & Hoffman, R. D. 1991, ApJ, 395, 202
Woosley, S. E., & Weaver, T. A. 1986a, in IAU Symp. 89, Radiation Hydrody-
  namics in Stars and Compact Objects, ed. D. Mihalas & K. H. Winkler
  (Berlin: Springer-Verlag), 92
———. 1986b, in ARA&A, Vol. 24, ed. G. Burbidge (Palo Alto: Annual
  Reviews), 205

Yakovlev, D. G. 1987, Soviet Astron., 31, 347
Yakovlev, D. G., & Urpin, V. A. 1980, Soviet Astron., 24, 303 (YU)
Zel'dovich, Ya. B., Barenblatt, G. I., Librovich, V. B., & Makhiladze, G. M.
  1985, The Mathematical Theory of Combustions and Explosions (New
  York: Plenum)